assigning phases in waves that vary strongly with height. The two sets of curves give markedly different results. Had damping times been estimated from amplitude ratios, yet different results would have been obtained.

For comparison, damping times computed for waves of the same periods using Spiegel's formula (100.17) are shown in Figure 102.5 as solid curves. The important conclusion to be drawn is that nonlocal effects resulting from radiative transfer produce *qualitatively* different propagation characteristics in a wave, and that it simply is not possible to reproduce these effects self-consistently with a single equivalent damping time.

STABILITY OF ACOUSTIC-GRAVITY WAVES IN A RADIATING FLUID

The possibility of radiation-driven instabilities in a stratified radiating atmosphere has been discussed by Berthomieu et al. (**B4**) and by Spiegel (**S19**). In the former paper, it is shown that above a certain critical frequency, isothermal, optically thin perturbations in an isothermal slab of an atmosphere traversed by a radiation field can be amplified by radiation in a drift instability. In the latter paper it is shown that under certain circumstances radiation forces can drive instabilities in a stratified radiating fluid. A detailed analysis is presented for quasi-adiabatic *photoacoustic* and *photogravity* modes. The results are intriguing, but it would take us too far afield to discuss them here; the interested reader should consult the original paper.

8.2 Nonlinear Flows

103. Thermal Waves

Thermal waves result from conductive energy-transport processes within a fluid, which give rise to an energy flux $q = -K \nabla T$. For nonradiating neutral gases it is usually satisfactory to assume *linear conduction* (K independent of T) because the conductivity depends only weakly on temperature (cf. §33). But in ionized plasmas where $K \propto T^{5/2}$, and in opaque radiating fluids where the radiation conduction coefficient depends strongly on T, we must treat *nonlinear conduction*. The distinction is important because thermal waves behave qualitatively differently in the two cases.

A problem of some interest in radiation hydrodynamics is the penetration of radiation from a hot source into cold material, a process that is reasonably well described by treating the radiation field in the diffusion approximation. Practical examples are the penetration of stellar radiation into the interstellar medium at the instant of star formation or of a supernova explosion, or the irradiation of a fusion pellet by intense laser beams. Such propagating radiation fronts are called *Marshak waves* (**M4**) or *radiation diffusion waves*.

Because radiative energy exchange is very efficient, significant radiation penetration and energy deposition can occur in a time much too short for

the fluid to be set into motion. In this section we therefore consider the penetration of radiation into a *static medium*. Eventually, of course, the material becomes hot, pressure gradients build, and the fluid flows; we examine the penetration of radiation into a moving medium in §106. In order to gain insight we will emphasize simple problems for which analytical solutions are possible, and then compare with numerical results obtained using techniques discussed in §97.

BEHAVIOR OF LINEAR CONDUCTION WAVES

In a static conducting fluid, the energy equation is

$$\rho c_v (\partial T/\partial t) = \mathbf{\nabla} \cdot (K \mathbf{\nabla} T). \tag{103.1}$$

Ignoring the spatial and temporal variation of K we can rewrite (103.1) as

$$(\partial T/\partial t) = \chi \nabla^2 T \tag{103.2}$$

where $\chi \equiv K/\rho c_v$ is the thermal diffusivity of the material. Equation (103.2) is to be solved subject to given initial and boundary conditions.

A classic problem is to solve (103.2) in one-dimensional planar geometry for an instantaneous heat pulse from a plane source in an infinite, cold $(T = 0)$ medium. Thus if we release $\mathcal{E}$ ergs cm^{-2} in the plane $x = 0$ at $t = 0$, we solve (103.2) with the initial condition

$$T(x, 0) = Q \, \delta(x) \tag{103.3}$$

and boundary conditions

$$T(\pm\infty, t) = 0. \tag{103.4}$$

By energy conservation

$$\int_{-\infty}^{\infty} T(x, t) \, dx = Q \equiv \mathcal{E}/\rho c_v \tag{103.5}$$

at all later times.

The well-known solution (**L2**, §51), (**M13**, 862) of this problem is

$$T(x, t) = [Q/(4\pi\chi t)^{1/2}] \exp(-x^2/4\chi t), \tag{103.6}$$

which is sketched in Figure 103.1a for various values of $\tau \equiv 4\chi t$. Equation (103.6) exhibits two important properties characteristic of linear conduction: (1) the bulk of the energy is contained within the region $|\Delta x| \lesssim (4\chi t)^{1/2}$, which shows that the range of energy penetration grows as $t^{1/2}$ (appropriate for a random-walk process). The peak temperature decreases as $t^{-1/2}$, as one also would expect from (103.5), which implies that $T_{\text{peak}} \Delta x \approx$ constant. (2) The process has an infinite signal speed in the sense that even at an infinitesimal time the temperature is nonzero for all x. The long-range tail, which contains only an infinitesimal amount of energy, results because the conductivity is finite everywhere, hence always admits a nonzero energy propagation no matter how low the temperature and how shallow the gradient.
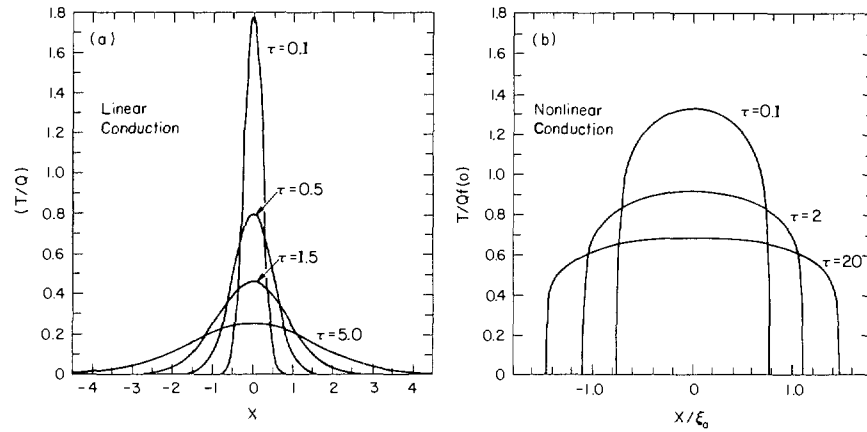
Fig. 103.1 Time development of temperature pulse for (a) linear and (b) nonlinear conduction.

BEHAVIOR OF NONLINEAR CONDUCTION WAVES

Suppose now that the conductivity is a function of temperature; in particular assume a power-law variation $K = K_0 T^n$, which allows K to increase sharply with rising temperature and to vanish at zero temperature. We must now solve

$$(\partial T/\partial t) = (\rho c_v)^{-1} \nabla \cdot (K_0 T^n \nabla T) \equiv \alpha \nabla \cdot (T^n \nabla T). \qquad (103.7)$$

Again suppose we apply an instantaneous heat pulse in the plane $x = 0$ of an infinite, cold medium. In this case heat cannot penetrate instantaneously to infinity because a finite amount of heat must first be deposited in the material to raise its conductivity above zero. The point at which the temperature first rises from zero, defining the position of the thermal wave, propagates into the medium with a finite velocity. Moreover because the conductivity, hence efficiency of heat transport, rises with rising temperature, we have a positive feedback mechanism that allows the temperature to rise very sharply from zero at a well-defined *thermal front*, behind which there is a nearly isothermal region extending back to the origin, as sketched in Figure 103.1b.

We can derive an exact solution for the problem just posed from a similarity analysis. The variables entering the problem are x [cm], t [s], and T [K]; in addition there are two parameters, Q [K cm] and α [cm^2 s^{-1} K^{-n}]. The only dimensionless combination that can be formed from x, t, α, and Q is

$$\xi \equiv x/(\alpha Q^n t)^{1/(n+2)} \qquad (103.8)$$

which we adopt as our similarity variable. It follows from (103.8) that the position of the front varies as $x_f \sim t^{1/(n+2)}$. The quantity $Q/(\alpha Q^n t)^{1/(n+2)} = (Q^2/\alpha t)^{1/(n+2)}$ has the dimensions of temperature, hence we seek a solution

of the form

$$T(x, t) = (Q^2/\alpha t)^{1/(n+2)} f(\xi) \tag{103.9}$$

where $f(\xi)$ is to be determined from (103.7).

From (103.8) we see that

$$(\partial f/\partial t) = -(n+2)^{-1}(\xi/t)(df/d\xi) \tag{103.10a}$$

and

$$(\partial f/\partial x) = (\alpha Q^n t)^{-1/(n+2)}(df/d\xi). \tag{103.10b}$$

Using (103.9) and (103.10) in (103.7) we derive an ordinary differential equation for f:

$$(n+2)\frac{d}{d\xi}\left(f^n\frac{df}{d\xi}\right) + \xi\frac{df}{d\xi} + f = 0. \tag{103.11}$$

The solution of this equation is (**L2**, 196), (**Z3**, 665)

$$f(\xi) = [n\xi_0^2/2(n+2)]^{1/n}[1-(\xi/\xi_0)^2]^{1/n} \tag{103.12}$$

for $\xi < \xi_0$, and $f(\xi) = 0$ for $\xi \geq \xi_0$. Here ξ_0 is a constant of integration that can be determined from the energy-conservation requirement (103.5), which, in view of (103.8) and (103.9), becomes

$$\int_{-\infty}^{\infty} f(\xi)\, d\xi = \int_{-\xi_0}^{\xi_0} f(\xi)\, d\xi = 1. \tag{103.13}$$

Evaluation of the integral gives

$$\xi_0^{n+2} = [(n+2)^{(n+1)}2^{(1-n)}/n\pi^{(n/2)}][\Gamma(\tfrac{1}{2}+1/n)/\Gamma(1/n)]. \tag{103.14}$$

From (103.8) the position of the thermal front is given by

$$x_f = \xi_0(\alpha Q^n t)^{1/(n+2)}. \tag{103.15}$$

The nonlinear conduction solution shown in Figure 103.1b is a plot of $T/Qf(0)$ for $n = 6$, as a function of x/ξ_0, for various values of $\tau \equiv \alpha Q^n t$.

MARSHAK WAVES

Let us now consider nonlinear radiation diffusion. We choose certain boundary conditions of interest in astrophysical applications and reserve the name "Marshak wave" for this particular class of problems. For static material, the energy equation in the equilibrium diffusion approximation is

$$\rho c_v(\partial T/\partial t) = \nabla \cdot (K_R \nabla T). \tag{103.16}$$

The rate of change of the radiation energy density has been neglected on the left-hand side, so the theory applies only when the fluid is not strongly radiation dominated.

From (97.3) the radiation conduction coefficient is

$$K_R = \tfrac{4}{3}a_R c\lambda_p T^3 = \tfrac{4}{3}a_R cT^3/\chi_R \tag{103.17}$$

where λ_p is the photon mean free path and χ_R is the Rosseland mean extinction coefficient. K_R is a very strong function of T because, for typical astrophysical materials, the Rosseland mean opacity scales as

$$\chi_R = \chi_0 \rho^\alpha T^{-n} \tag{103.18}$$

where n is about 3.5 [cf. (**C23**, 378–380), (**S10**, 68–70)]. Hence K_R typically varies as T^6 or T^7, and even more rapidly under certain circumstances.

A complete discussion of one-dimensional radiation diffusion for the case of a constant driving temperature at the plane $x = 0$ has been given by Petschek, Williamson, and Wooten (**P2**); see also (**K4**). In their notation we wish to solve

$$(\partial T/\partial t) = \mathcal{K}(\partial^2 T^m/\partial x^2) \tag{103.19}$$

where

$$\mathcal{K} \equiv (4a_R c/3m)/(\chi_0 c_v \rho^{\alpha+1}) \tag{103.20}$$

and

$$m \equiv n + 4, \tag{103.21}$$

subject to the condition $T \equiv T_0$ at $x = 0$.

Adopting the similarity variable

$$\xi \equiv x/(2\mathcal{K}T_0^{m-1} t)^{1/2} \equiv Ax/t^{1/2}, \tag{103.22}$$

which implies

$$(\partial f/\partial t) = -\tfrac{1}{2}(\xi/t)(df/d\xi) \tag{103.23a}$$

and

$$(\partial^2 f/\partial x^2) = (A^2/t)(d^2 f/d\xi^2), \tag{103.23b}$$

and adopting the scaled temperature

$$\tau(x, t) \equiv T(x, t)/T_0$$

as dependent variable, we can rewrite (103.19) as

$$(d^2 \tau^m/d\xi^2) = -\xi(d\tau/d\xi). \tag{103.24}$$

The boundary conditions are $\tau \equiv 1$ at $\xi = 0$, and $\tau = (d\tau^m/d\xi) = 0$ at some point ξ_0 yet to be determined. The latter implies that the flux vanishes at ξ_0 because

$$F = -K_R(\partial T/\partial x) = -\rho c_v(\mathcal{K}T_0^{m+1}/2t)^{1/2}(d\tau^m/d\xi). \tag{103.25}$$

The total energy in the wave is

$$\mathcal{E} = \rho c_v \int_0^{x_v} T\, dx = \rho c_v(2\mathcal{K}T_0^{m-1} t)^{1/2} \varepsilon \tag{103.26}$$

where

$$\varepsilon \equiv \int_0^{\xi_0} \tau\, d\xi. \tag{103.27}$$

Table 103.1. Properties of Marshak Waves

		ξ_0		ε	
n	m	Exact	Approximate	Exact	Approximate
0.0	4.0	1.231	1.118	0.940	0.894
1.0	5.0	1.177	1.095	0.952	0.913
2.0	6.0	1.143	1.080	0.960	0.926
2.5	6.5	1.130	1.074	0.963	0.931
3.0	7.0	1.120	1.069	0.965	0.935
3.5	7.5	1.111	1.065	0.968	0.939
4.0	8.0	1.103	1.061	0.970	0.943
5.0	9.0	1.091	1.054	0.973	0.949
10.0	14.0	1.057	1.035	0.982	0.966

Energy conservation implies that $(\partial \mathscr{E}/\partial t) = F(x = 0, t)$, which is equivalent to

$$\varepsilon = -(d\tau^m/d\xi)_{\xi=0}, \tag{103.28}$$

a result needed below.

After appropriate transformation, (103.24) is readily integrated numerically. For a given n, hence m, the solution yields ξ_0, ε, and $\tau(\xi)$; extensive results are tabulated in (**P2**). A few representative values are summarized in Table 103.1. Petschek et al. also develop a hierarchy of approximate analytical solutions starting from the zeroth approximation $\tau(\xi) \equiv 1$ for $0 \le \xi \le \xi_0$ and zero for $\xi > \xi_0$, which implies that $\xi_0 = 1$ and $\varepsilon = 1$. Another approximate solution is obtained by making the *constant flux approximation*, demanding that the net flux be constant behind the wave front so that

$$(d\tau^m/d\xi) = -C \tag{103.29}$$

for $0 \le \xi \le \xi_0$. Integrating from ξ to ξ_0 we have

$$\tau^m = C\xi_0[1 - (\xi/\xi_0)]. \tag{103.30}$$

But $\tau(0) \equiv 1$, hence $C = 1/\xi_0$. Furthermore, from (103.27)

$$\varepsilon = \int_0^{\xi_0} [1 - (\xi/\xi_0)]^{1/m} \, d\xi = \xi_0 m/(m + 1), \tag{103.31}$$

which, when used in (103.28) with $(d\tau^m/d\xi) = -1/\xi_0$ from (103.29), yields

$$\xi_0 = [(m + 1)/m]^{1/2}. \tag{103.32}$$

The values of ξ_0 and ε obtained from (103.32) and (103.31) are compared with the exact values in Table 103.1; the error in ξ_0 is at most 10 percent and in ε at most 5 percent, so the approximation is useful. Petschek et al. call this the "one-halfth" approximation because it is intermediate in accuracy between the zeroth and first approximations of their hierarchy.
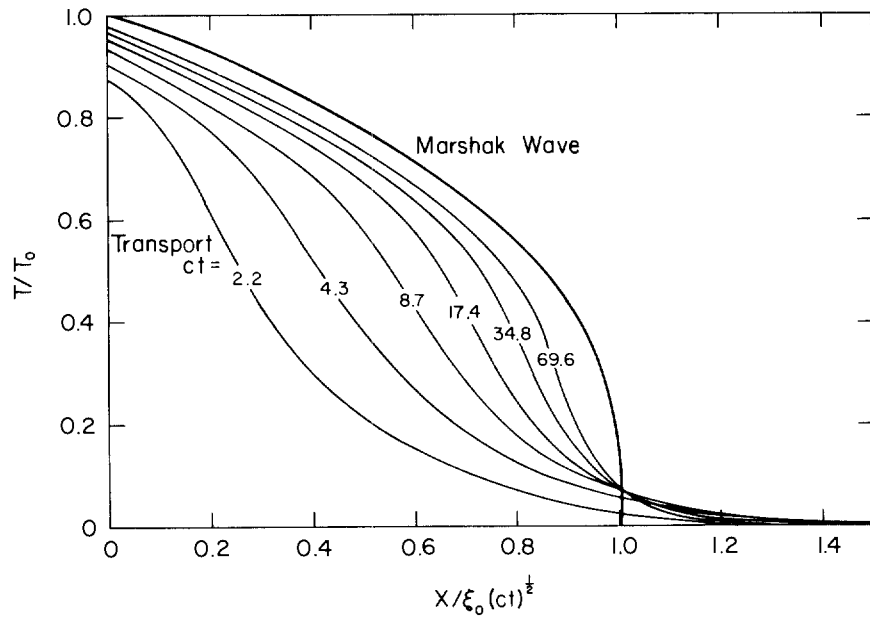
COMPARISON WITH NONEQUILIBRIUM DIFFUSION AND TRANSPORT

Comparisons of the Marshak-wave similarity solution with nonequilibrium diffusion and full transport calculations are reported in (B1) and (C1). In these calculations the temperature dependence of the opacity is ignored but the rate of change of the radiation energy density is included, so the equation solved is

$$\frac{\partial}{\partial t}(\rho c_v T + a_R T^4) = \tfrac{1}{3}a_R c\lambda_p \frac{\partial^2 T^4}{\partial x^2} .$$ (103.33)

If both x and ct are measured in units of λ_p, the problem depends on only one dimensionless parameter, $\eta \equiv a_R T_0^3/\rho c_v$. Equation (103.33) is solved by transforming to the new variable $\xi \equiv x/(ct)^{1/2}$ and by integrating the resulting ordinary differential equation for $\tau \equiv \eta(T/T_0)^4$ numerically. The value of ξ_0 at the front depends only on η. The transport solution is effected by a discrete-ordinate solution of the time-dependent transfer equation in (B1) and by a Monte Carlo simulation in (C1).

Results obtained from imposing the boundary condition $T(x = 0, t) \equiv T_0$ are shown in Figure 103.2 for a case with $\eta = 1.69$ (which implies $\xi_0 = 1.06$). In this plot the Marshak wave is represented by a single curve, whereas the shape of the transport solution evolves in time. The Marshak wave always deposits too much energy into the material and significantly

Fig. 103.2 Comparison of Marshak wave with transport solution for radiation penetration into a cold medium. From (B1).
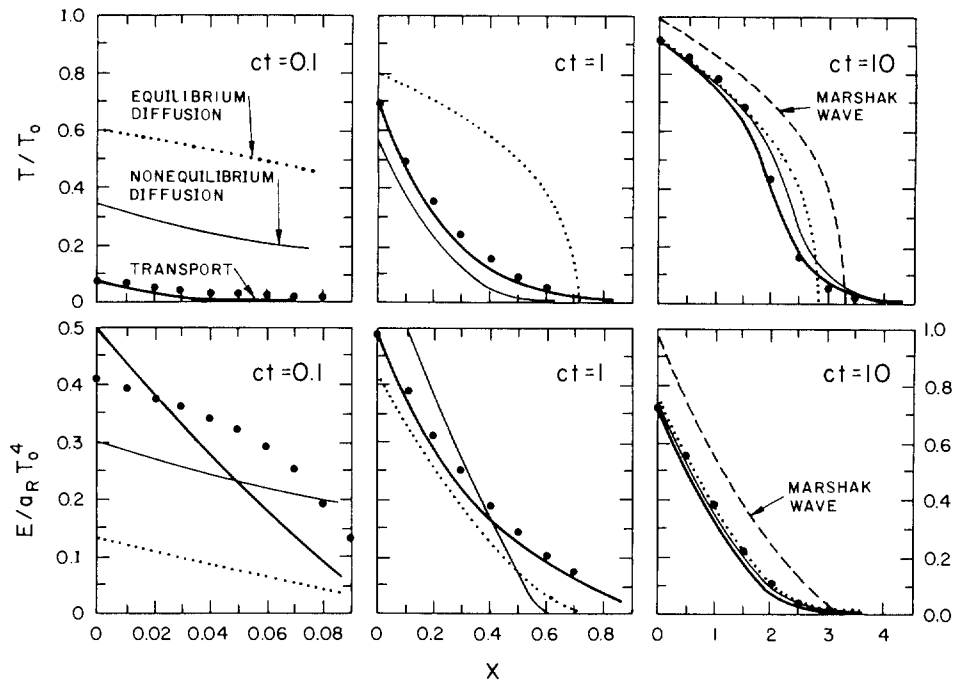
Fig. 103.3 Comparison of equilibrium diffusion, nonequilibrium diffusion, and transport solutions for radiation penetrating into cold material. From (**C1**). Heavy dots show results from an unpublished flux-limited diffusion calculation, kindly communicated by Dr. C. D. Levermore.

outruns the real radiation front (except for the exponentially attenuated tail of photons that have entered the slab at normal incidence and have penetrated to a depth $x = ct$). The too-rapid heating of the material is shown vividly in Figure 103.3 where the Marshak front can be plotted on the graphs only for $ct = 10$; at earlier times it is off the right edge of the graph: at $x = 0.335$ for $ct = 0.1$ and $x = 1.06$ at $ct = 1$.

The solution can be improved considerably by choosing a better boundary condition. In reality the material at $x = 0$ does not equilibrate instantaneously to $T = T_0$, but reaches this temperature only after a finite time. Thus our constant-temperature boundary condition forces the radiative conductivity to be too large from the outset, thereby admitting too large a flux, hence rate of energy deposition. A more accurate description of the physics is to assume a *constant imposed radiation field* $I(x = 0, \mu) \equiv I^- = B(T_0) = (a_R c/4\pi)T_0^4$ for $-1 \le \mu \le 0$. Now from (83.12), (83.13), and (83.15) we have

$$\mu^2(\partial j/\partial \tau)|_{x=0^+} = \mu h(x = 0^+) = \mu[j(x = 0^+) - I^-], \qquad (103.34)$$

which, when integrated over angle $(0 \leq \mu \leq 1)$ yields

$$-\tfrac{1}{3}\lambda_p(\partial J/\partial x)|_{x=0^+} = \tfrac{1}{2}[J(x=0^+) - I^-].$$ (103.35)

But $J(x=0) = (c/4\pi)E(x=0) = (a_R c/4\pi)[T(x=0)]^4$, hence we have the boundary condition

$$[\tfrac{1}{2}T^4 - \tfrac{1}{3}\lambda_p(\partial T^4/\partial x)]_{x=0} = \tfrac{1}{2}T_0^4.$$ (103.36)

With (103.36) as the boundary condition, it is no longer possible to solve the problem with a similarity transformation like that used earlier. Instead, (103.33) and (103.36) are solved numerically using the techniques described in §97; the results are denoted "equilibrium diffusion approximation" in Figure 103.3.

Although more accurate than the Marshak wave, the equilibrium diffusion solution still yields too much material heating and too low a radiation density at early times. The results can be improved further by using the nonequilibrium diffusion approximation of §97, which allows the material and the radiation field to have different temperatures. As seen in Figure 103.3 we now obtain a larger radiation energy density and a lower material temperature, in much better agreement with transport theory; indeed for $ct \geq 1$ the material temperature profile is reasonably accurate. The non-equilibrium diffusion results are still in serious error during the earliest instants because (1) the radiation field is assumed to be isotropic and (2) the energy transport is not flux limited. Substantially better results at the earliest times are obtained using flux-limited diffusion (cf. §97).

OTHER SOLUTIONS

Analytical solutions exist for a variety of other nonlinear radiation diffusion problems. For example, Marshak (**M4**) obtained similarity solutions for radiation penetration when T_0 varies as t^α or as exp (αt). Zel'dovich and Raizer give a similarity solution for nonlinear heat conduction (or radiation diffusion) from an instantaneous point source in spherical geometry (**Z3,** 668), and for a slab with a constant *net* (as opposed to *incident*) flux at the boundary (**Z3,** 673). Pomraning (**P3**) solved the non-self-similar problem of the diffusion of radiation from a cavity using a moments method for plane, cylindrical, and spherical geometries. His solution reproduces the exact results in both the early- and late-time limits.

104. Steady Shocks

One of the most interesting phenomena in radiation hydrodynamics is the *radiating shock,* which occurs in a wide variety of astrophysical flows. In this section we consider *steady* radiating shocks, which can arise in steady flows (e.g., stellar winds or accretion flows), and which also can be used as

an instantaneous description of propagating shocks when the shock thickness is very small compared to a characteristic length over which the ambient medium changes significantly (e.g., a scale height). As in Chapter 5, we first treat the shock as a discontinuity and derive jump relations that relate the equilibrium states of the upstream and downstream material far from the front; we then consider the structure of the front itself in greater detail.

RANKINE–HUGONIOT RELATIONS FOR A RADIATING SHOCK

Consider a steady, one-dimensional, planar flow of a radiating fluid. Our main goal here is to account for the effects of the radiation energy density, pressure, and energy flux, so we ignore viscosity and thermal conduction and assume the material to be a perfect gas. The flow is then governed by the equation of continuity

$$(\partial \rho / \partial t') + [\partial (\rho v) / \partial x'] = 0, \tag{104.1}$$

momentum [cf. (96.5)]

$$[\partial (\rho v) / \partial t'] + [\partial (\rho v^2 + p + P_0) / \partial x'] = 0, \tag{104.2}$$

and energy [cf. (96.15)]

$$[\partial (\rho e + \tfrac{1}{2} \rho v^2 + E_0) / \partial t'] + \{\partial [\rho v (h + \tfrac{1}{2} v^2) + F_0 + v(E_0 + P_0)] / \partial x'\} = 0, \tag{104.3}$$

where (x', t') denote lab-frame coordinates with respect to which the shock moves with velocity v_S. In (104.2) we have dropped two terms containing F_0, which are $O(\lambda_p v / l c)$ in the diffusion limit, and at most $O(v/c)$ in the streaming limit, compared to $(\partial P_0 / \partial x')$, hence are negligible for non-relativistic flow speeds.

It is straightforward to show that (104.1) to (104.3) are invariant under the Galilean transformation

$$x \equiv x' - v_S t', \qquad t' \equiv t, \qquad u \equiv v - v_S \tag{104.4}$$

to the frame in which the shock front is stationary. Thus we obtain shock-frame conservation relations by making the substitutions $(\partial / \partial t') \rightarrow (\partial / \partial t)$, $(\partial / \partial x') \rightarrow (\partial / \partial x)$, and $v \rightarrow u$. Furthermore, in this frame the flow is steady, so we can drop terms in $(\partial / \partial t)$ obtaining

$$d(\rho u)/dx = 0, \tag{104.5}$$

$$d(\rho u^2 + p + P_0)/dx = 0, \tag{104.6}$$

and

$$d[\rho u(h + \tfrac{1}{2} u^2) + F_0 + u(E_0 + P_0)]/dx = 0. \tag{104.7}$$

Integrating (104.5) to (104.7) across the front, and formally taking the

limit of vanishing shock thickness as in §56, we obtain the *radiation-modified Rankine–Hugoniot jump conditions*

$$\rho_1 u_1 = \rho_2 u_2 \equiv \dot{m}, \qquad (104.8)$$

$$\dot{m} u_1 + p_1 + P_{01} = \dot{m} u_2 + p_2 + P_{02}, \qquad (104.9)$$

$$\dot{m}(h_1 + \tfrac{1}{2} u_1^2) + F_{01} + u_1 (E_{01} + P_{01}) = \dot{m}(h_2 + \tfrac{1}{2} u_2^2) + F_{02} + u_2 (E_{02} + P_{02}), \qquad (104.10)$$

results first derived by Marshak (**M4**). As usual the subscripts "1" and "2" denote upstream and downstream conditions, respectively.

Comparing (104.8) to (104.10) with (56.6) to (56.8) we see that the gas pressure and the material enthalpy density are replaced by the total pressure $(p + P_0)$ and total enthalpy density $e + (p + E_0 + P_0)/\rho$. More significant, in contrast to a nonradiating shock [in which the conduction flux, proportional to (dT/dx), necessarily vanishes far from the shock front where there are no gradients] we now may have a nonvanishing radiation flux in both the upstream and downstream flow owing to *nonlocal transport* of radiant energy into optically thin material. Generally speaking, the radiation energy density and pressure are important only at extremely high temperatures (hence for very strong shocks) and/or low densities, whereas radiative energy exchange plays a fundamental role in all radiating shocks.

Note that all radiation quantities in (104.9) and (104.10) are evaluated in the comoving fluid frame on both sides of the jump. By virtue of (91.17) we can rewrite (104.10) in terms of the radiation flux measured in the frame in which the shock is at rest:

$$\dot{m}(h_1 + \tfrac{1}{2} u_1^2) + F_1 = \dot{m}(h_2 + \tfrac{1}{2} u_2^2) + F_2. \qquad (104.11)$$

In practice (104.10) is more useful in opaque material where we can use the diffusion approximation, and (104.11) is more useful for transparent material where, if we ignore velocity-dependent terms in the transfer problem, we can write the flux in terms of the Φ operator (cf. §79) operating on the material source function.

It is instructive to analyze the jump conditions (104.8) to (104.10) in two limiting regimes:

(*a*) *Opaque Material* · Suppose first that both the upstream and the downstream material is extremely opaque. Then any radiation crossing the front from the hot downstream material into the cooler upstream material will be completely reabsorbed within a thin layer into which it can penetrate by diffusion. To estimate the thickness of this layer we equate the time $t_d = (l/\lambda_p)^2 (\lambda_p/c)$ required for the radiation to diffuse a distance l from the front, to the time $t_f = (l/v)$ required for this material to be swept back into the shock front, obtaining

$$l \sim (c/v) \lambda_p. \qquad (104.12)$$

The radiation diffusion layer cannot grow much beyond the thickness given by (104.12) because t_d increases quadratically with l, but t_f only linearly.

Outside the diffusion layer conditions again become homogeneous and the radiation flux vanishes. Hence at sufficiently large distances from the shock $F_{01} = F_{02} = 0$, and (104.10) simplifies to

$$\dot{m}(h_1 + \tfrac{1}{2}u_1^2) + u_1(E_{01} + P_{01}) = \dot{m}(h_2 + \tfrac{1}{2}u_2^2) + u_2(E_{02} + P_{02}). \quad (104.13)$$

This expression is appropriate for very high-temperature flows (e.g., in a stellar envelope) where the contributions of the radiation pressure and energy density are significant.

Suppose now that the material component of the fluid is a completely ionized plasma, so that $p = \rho kT/\mu_0 m_{\rm H} \equiv \rho RT$ with μ_0 constant and $\gamma = \tfrac{5}{3}$, and that the radiation is in equilibrium with the material so that $E_0 = 3P_0 = a_R T^4$. Then (104.8), (104.9), and (104.13) completely determine downstream conditions for given upstream conditions. Defining the compression ratio

$$r \equiv \rho_2/\rho_1 = u_1/u_2 \quad (104.14)$$

we can rewrite (104.9) and (104.13) in nondimensional form:

$$\gamma M_1^2(r-1)/r = (\Pi - 1) + \alpha_1[(\Pi/r)^4 - 1] \quad (104.15)$$

and

$$\tfrac{1}{2}\gamma M_1^2(r^2 - 1)/r^2 = [\gamma/(\gamma - 1)][(\Pi/r) - 1] + 4\alpha_1[(\Pi^4/r^5) - 1] \quad (104.16)$$

where

$$\Pi \equiv p_2/p_1, \quad (104.17)$$

$$\alpha_1 \equiv \tfrac{1}{3}a_R T_1^4/p_1, \quad (104.18)$$

and

$$M_1 \equiv u_1/a_1 = u_1(\rho_1/\gamma p_1)^{1/2}. \quad (104.19)$$

Note that for $\alpha_1 \equiv 0$, that is, no radiation pressure, (104.15) and (104.16) reduce to (56.9) and (56.17).

To solve the nonlinear system (104.15) and (104.16) we regard r as the independent variable and α_1 as a given parameter. Eliminating M_1^2 between (104.15) and (104.16) we obtain

$$\alpha_1 r^{-4}(7 - r)\Pi^4 = (r - r_0)\Pi + \alpha_1(7r - 1) + (r_0 r - 1) \quad (104.20)$$

where

$$r_0 \equiv (\gamma + 1)/(\gamma - 1) \quad (104.21)$$

is the maximum compression ratio for a strong shock in a nonradiating gas; for $\gamma = \tfrac{5}{3}$, $r_0 = 4$. Equation (104.20) yields $\Pi(r, \alpha_1)$; given Π we find $M_1(r, \alpha_1)$ from either (104.15) or (104.16). These results can then be inverted to find $r(M_1, \alpha_1)$, hence $\Pi(M_1, \alpha_1)$.

In general (104.20) must be solved numerically. However it is obvious

that as $r \to 7$, the limiting compression ratio for a gas with $\gamma = \frac{4}{3}$ (e.g., pure radiation), we obtain an infinitely strong shock with $\Pi \propto (7-r)^{-1/3} \to \infty$ and $M_1 \propto \Pi^2 \propto (7-r)^{-2/3} \to \infty$. Because the compression ratio is essentially fixed in very strong shocks, $T_2/T_1 \approx p_2/p_1 = \Pi$, whence we see that in a very strong radiating shock the temperature ratio grows only as $M_1^{1/2}$; in contrast, in a nonradiating shock it rises as M_1^2 [cf. (56.42)].

For a weak shock with $r = 1 + \xi$, where $\xi \ll 1$, one finds from (104.20) that $\not{p} \equiv [(p_2/p_1) - 1]$ is

$$\not{p} = \xi(r_0 + 1 + 32\alpha_1)/(r_0 - 1 + 24\alpha_1) \to \xi(5 + 32\alpha_1)/(3 + 24\alpha_1), \quad (104.22)$$

where the second expression holds for $\gamma = \frac{5}{3}$. Equation (104.22) yields $\not{p} = \Gamma\xi$ [cf. (56.36)] with $\Gamma = \gamma = \frac{5}{3}$ when $\alpha_1 = 0$, and $\Gamma \to \frac{4}{3}$ as $\alpha_1 \to \infty$. Furthermore, one finds from (104.15) and (104.22) that

$$M_1^2 \approx (5 + 40\alpha_1 + 32\alpha_1^2)/(5 + 40\alpha_1). \quad (104.23)$$

This is the expected result because in a weak shock u_1 must equal $[\Gamma_1(1 + \alpha_1)p_1/\rho_1]^{1/2}$, the sound speed of the radiating fluid, hence $M_1^2 \equiv u_1^2/a_{\text{gas}}^2 = \Gamma_1(1 + \alpha_1)/\gamma$, which, in light of (70.22) for Γ_1, yields (104.23).

An explicit analytical solution can be obtained for the limiting case of a very strong shock propagating into a cold gas (**S2**). We neglect the gas and radiation energy densities and pressures in the upstream material, which is equivalent to dropping unity wherever it appears on the right-hand sides of (104.15) and (104.16). Eliminating M_1^2 between these two equations we obtain

$$\alpha_1\Pi^3 = r^4(r - r_0)/(7 - r): \quad (104.24)$$

Reverting to dimensional variables we have

$$T_2^3 = (3R\rho_1/a_R)r(r - r_0)/(7 - r) \quad (104.25)$$

which yields $T_2(r)$. Given T_2 we can immediately compute p_2 and P_2. Using (104.24) in the simplified version of (104.15) we find

$$M_1^2 = \Pi r(r - r_0)/\gamma(r - 1)(7 - r). \quad (104.26)$$

Note that (104.24) to (104.26) are valid only for r appreciably larger than r_0.

(*b*) *Optically Thin Upstream Material* Suppose now that we have a radiating shock propagating into optically thin upstream material. Focusing mainly on the effects of radiative energy transport across the front, we assume the flow to be cool enough that we can neglect the radiation energy density and pressure. The radiation-modified jump conditions reduce to (56.6), (56.7), and

$$\dot{m}(h_1 + \tfrac{1}{2}u_1^2) + F_{01} = \dot{m}(h_2 + \tfrac{1}{2}u_2^2) + F_{02}. \quad (104.27)$$

We focus on the case of a nonzero net flux across the front, that is,

$|F_{01} - F_{02}| > 0$, which will occur if the preshock material is sufficiently transparent that radiation originating in the hot postshock material (which may be so opaque that $F_{02} \approx 0$) can flow freely across the front and escape to infinity upstream (implying a large value for $|F_{01}|$). An example is a strong shock emerging from the photosphere or chromosphere of a star.

By an analysis similar to that leading to (56.20) and (56.21), we find

$$\frac{\rho_2}{\rho_1} = \frac{[(\gamma+1)p_2+(\gamma-1)p_1]u_2+2(\gamma-1)(F_{02}-F_{01})}{[(\gamma+1)p_1+(\gamma-1)p_2]u_2} \qquad (104.28)$$

and

$$\frac{T_2}{T_1} = \left(\frac{p_2}{p_1}\right)\frac{[(\gamma+1)p_1+(\gamma-1)p_2]u_1+2(\gamma-1)(F_{01}-F_{02})}{[(\gamma+1)p_2+(\gamma-1)p_1]u_1} . \qquad (104.29)$$

For the geometry sketched in Figure 55.2 the shock is moving to the left in the lab frame, hence both u_1 and u_2 are positive in the shock's frame, whereas a net radiation flux into the cooler upstream material implies that $(F_{01} - F_{02}) < 0$ (i.e., a net flow of energy to the left). Therefore a net flow of radiant energy upstream decreases the temperature jump and increases the density jump. The upstream material is preheated by a *radiation precursor*, and the downstream material is cooled by radiative losses.

In more general terms, the example just discussed illustrates that radiative energy transport across a shock can significantly alter the temperature, density, and velocity profiles in both the upstream and downstream flow over distances determined by the opacity of the material. To analyze these effects in more detail we must now examine the *structure* of radiating shocks.

EQUATIONS OF RADIATING SHOCK STRUCTURE

Adding material viscosity and heat-conduction terms to (104.2) and (104.3), and transforming to the frame of the shock, we obtain general conservation relations which apply throughout the flow. As before, these admit first integrals, that is, (104.8) and

$$\dot{m}u + p + P_0 - \mu'(du/dx) = \dot{m}C_1 = \text{constant}, \qquad (104.30)$$

and

$$\dot{m}(h + \tfrac{1}{2}u^2) + F_0 + u(E_0 + P_0) - \mu'u(du/dx) - K(dT/dx) = \dot{m}C_2^2 = \text{constant}, \qquad (104.31)$$

where $\mu' \equiv (\tfrac{4}{3}\mu + \zeta)$ is the effective one-dimensional viscosity.

Equations (104.30) and (104.31) show that in principle the structure of a radiating shock is determined by the combined action of viscosity, thermal conduction, and radiative energy transport. But in practice, photon mean free paths are orders of magnitude larger than particle mean free paths. Hence the viscous-conduction dissipation zone, which is only a few particle

mean free paths thick, can be considered to be a mathematical discontinuity across which we allow discrete jumps in temperature, density, pressure, and velocity according to the usual Rankine–Hugoniot relations while the radiation quantities E_0, F_0, and P_0 remain continuous. This discontinuity is embedded in the *radiation exchange zone*, whose thickness is a few to many photon mean free paths, which determines the largest-scale structure of the shock front. We therefore drop the material viscosity and conductivity terms henceforth.

The same remarks apply to the material relaxation zone discussed in §57 as long as the material is assumed to be in LTE, for then the characteristic relaxation length is of the same general size as a particle mean free path, hence is much less than λ_p. As we will see, however, the assumption of LTE is often invalid, particularly in strong shocks where radiation from the hot postshock region is markedly out of equilibrium with the cool preshock material and can therefore drive it out of LTE. Moreover, equilibrium in the downstream material cannot be recovered until the shocked gas has time to recombine and radiate; in fact the size of the material ionization-relaxation zone is of the same order as the size of the radiation-exchange zone. Despite these caveats it is very instructive to analyze shock structure under the assumption of LTE, and we therefore do so in some detail before discussing non-LTE effects, which must be treated numerically.

From a different point of view, we can consider radiation exchange as a mechanism for producing partly or completely dispersed shocks. Unlike the relaxation processes discussed in §57 (but like thermal conduction by electrons), radiation produces not only a tail but also a precursor in the flow. If the shock is not too strong, the tail and precursor can join, giving a completely dispersed continuous solution. With increasing shock strength, a regime is reached in which a continuous solution is not possible; instead, there is a temperature discontinuity at the front, followed by a significant temperature overshoot, as is characteristic of a partly dispersed solution. Beyond a certain critical shock strength, the radiative flux causes this downstream overshoot to collapse to a sharp spike whose thickness is less than one photon mean free path. Finally, for extremely strong shocks (and/or sufficiently hot upstream material) in which the radiation pressure and energy density dominate over the material contributions, continuous solutions are again possible.

APPROXIMATE ANALYSIS OF STRONG SHOCKS WITH NONEQUILIBRIUM
RADIATION DIFFUSION

The penetrating phenomenological discussions by Zel'dovich and Raizer (**Z1**), (**Z2**), (**R1**), (**Z3,** Chap. 7) offer considerable insight into the behavior of radiating strong shocks. To make the problem tractable analytically we assume the following. (1) A strong shock propagates into cold material, which implies that we can neglect the upstream pressure and energy density. (2) The material (a perfect gas) remains in LTE with all species of

particles at the same kinetic temperature. (3) The radiation field can be treated in the nonequilibrium diffusion approximation. (4) The shock is in an optically thick medium and all radiation emanating from the front is reabsorbed in the upstream material, so that we have a closed thermodynamic system (no open boundaries). (5) It suffices to account for the radiative energy flux, whereas the radiation pressure and energy density can be ignored.

(a) *Basic Equations*   Under the assumptions stated above the momentum and energy conservation relations (104.30) and (104.31) reduce to

$$\dot{m}u + p = \dot{m}u_1 \tag{104.32}$$

and

$$\dot{m}(h + \tfrac{1}{2}u^2) + F = \tfrac{1}{2}\dot{m}u_1^2. \tag{104.33}$$

The radiation field is governed by

$$(dF/d\tau) = 4\pi B - cE \tag{104.34}$$

and

$$F = -\tfrac{1}{3}c(dE/d\tau) \tag{104.35}$$

where $B = \sigma_R T^4/\pi$, and τ is the optical depth measured in the positive x direction, $d\tau \equiv \kappa\, dx$, with $\tau = 0$ chosen at the shock front. Combining (104.34) and (104.35) we have

$$(d^2F/d\tau^2) = 3F + 16\sigma_R T^3(dT/d\tau). \tag{104.36}$$

We have dropped the subscript "0" on radiation quantities because (104.34) to (104.36) are not correct comoving-frame equations; they are only approximate inasmuch as all velocity-dependent terms (such as the rate of work done by radiation pressure and the advection of radiation energy density) are omitted. These omissions are not serious for our present purposes, and in fact are consistent with the assumption that we can neglect E_0 and P_0 in the fluid conservation relations.

Equations (104.34) to (104.36) are to be solved subject to the boundary conditions $F_1 = E_1 = T_1 = 0$ at $\tau = -\infty$, and $F_2 = 0$, $T = T_2$, $E_2 = 4\pi B/c = a_R T_2^4$ at $\tau = +\infty$, which follow from assumptions (1) and (4) stated above. In terms of the volume ratio $\eta \equiv \rho_1/\rho$, (104.32) becomes

$$p = \dot{m}u_1(1 - \eta). \tag{104.37}$$

Using the perfect gas law for p we have

$$T/T_2 = \eta(1 - \eta)/\eta_2(1 - \eta_2), \tag{104.38}$$

hence from (104.33) we obtain

$$F = -\dot{m}RT(\eta - \eta_2)/2\eta\eta_2 \tag{104.39a}$$

$$= -\dot{m}RT_2(1 - \eta)(\eta - \eta_2)/2\eta_2^2(1 - \eta_2). \tag{104.39b}$$

Here $\eta_2 = (\gamma - 1)/(\gamma + 1)$ is the limiting volume ratio for an infinitely strong shock; $\eta_2 = \frac{1}{4}$ for $\gamma = \frac{5}{3}$. $T(\eta)$ and $F(\eta)$ are sketched in Figure 104.2.

(b) *Subcritical Shocks*   If a shock in cold material is very weak, radiation has negligible influence on the energy balance, and we obtain the usual step discontinuities characteristic of an adiabatic shock in an ideal fluid. With increasing shock strength T_2 rises, and the radiation flux across the front (which can be estimated roughly as the flux $\sigma_R T_2^4$ emitted from an opaque "wall" of postshock material at temperature T_2) increases very rapidly. This radiation is absorbed in the upstream material and heats it to some characteristic temperature T_- immediately in front of the shock; the precursor decays away exponentially upstream as the radiation attenuates in the preshock material. As we will see below, T_- is proportional to the radiation flux incident from the postshock material, and thus rises rapidly as T_2 increases, eventually equaling T_2. Shocks with $T_- < T_2$ are called *subcritical*. Because material entering the shock is preheated, the postshock temperature T_+ overshoots its final equilibrium value T_2. The overshoot decays downstream as the material cools by emitting photons that penetrate across the shock.

In short, radiation acts as a thermodynamic heat-transfer mechanism from hot to cold material in the flow. The resulting shock structure is sketched in Figure 104.1. Preheating produces a small pressure and density rise in the upstream material. Downstream the pressure increases only a small amount from its postshock value; the density shows a larger fractional rise because the downstream material cools while the pressure rises.

From (104.38) one sees that η must always be quite close to unity in the preshock material; indeed, even if T_- is as large as T_2, still $\eta_- = (1 - \eta_2) = 0.75$ for $\gamma = \frac{5}{3}$. Thus in the upstream flow we can set $\eta \approx 1$, and from (104.39) we have

$$F = -\dot{m}RT/(\gamma - 1) = -\dot{m}e, \qquad (104.40)$$

which has a straightforward physical interpretation: at any position in front of the shock, the material internal energy flux flowing downstream just equals the radiant flux flowing upstream because all the radiant energy passing that position is absorbed upstream and goes into heating the gas (nominally from zero temperature).

When T_- is appreciably smaller than T_2, we can derive an approximate solution for the structure of the precursor. The thermal energy density $a_R T_-^4$ will be much smaller than the energy density in the radiation field emerging from the shock (which is of order $a_R T_2^4$) hence we can make the simplifying assumptions that we can neglect B in (104.34) and drop the last term from (104.36), obtaining

$$F = F_0 e^{-\sqrt{3}|\tau|} \qquad (104.41)$$

and

$$E = -(\sqrt{3}/c)F = -(\sqrt{3}/c)F_0 e^{-\sqrt{3}|\tau|}. \qquad (104.42)$$
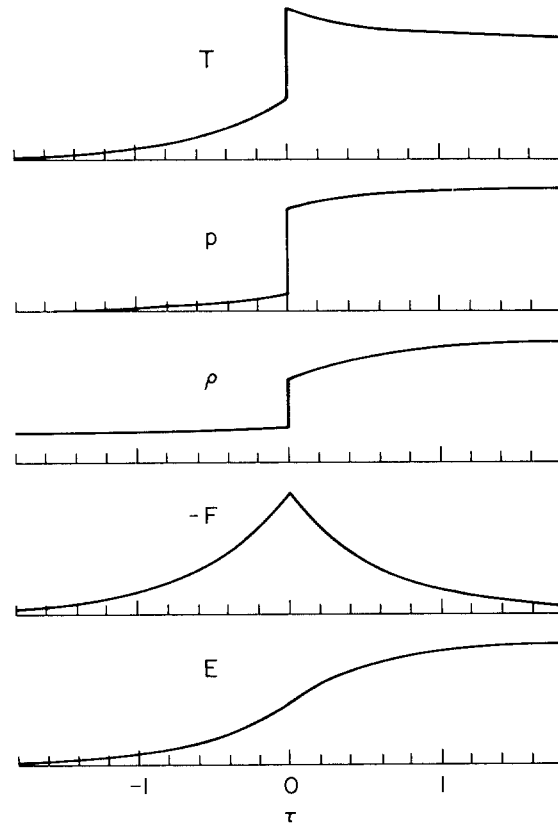
Fig. 104.1 Distribution of temperature, pressure, density, radiation flux, and radiation energy density as a function of optical depth in a subcritical shock.

(Recall that $F<0$ and $\tau<0$ upstream from the shock.) In (104.41) and (104.42) F_0 is the flux at the shock front; we fix its value in terms of T_2 below. Clearly the radiation field in the precursor is severely out of equilibrium.

Using (104.41) in (104.40) we find

$$T = T_- e^{-\sqrt{3}|\tau|}. \tag{104.43}$$

Because the preshock density variation is small, $p \propto T$ hence

$$p = p_- e^{-\sqrt{3}|\tau|}. \tag{104.44}$$

Equations (104.44) and (104.37) imply that

$$\rho - \rho_1 \approx (\rho_- - \rho_1)e^{-\sqrt{3}|\tau|}. \tag{104.45}$$

To develop an approximate solution for the structure of the postshock tail, we first note that both the radiation energy density and the flux must

be continuous across the shock front. This result was proved rigorously by Zel'dovich (**Z1**) and is also intuitively obvious from the fact that both E and F are integrals of the source function against well-behaved weight functions. Only if B were *singular* (not merely discontinuous) could we produce discontinuities in E and F, but such singularities are physically inadmissible. Furthermore, (1) if the energy density were discontinuous, (104.35) would imply that the flux is somewhere infinite, whereas by energy conservation it must remain finite. (2) If the flux were discontinuous then (104.34) would imply an infinite net absorption-emission rate at some point in the flow, which is physically nonsensical.

Next we argue that in the postshock material $T \approx T_2$, hence $\pi B \approx \sigma_R T_2^4 = $ constant. From (104.36) we then have

$$F = F_0 e^{-\sqrt{3}\,\tau}, \tag{104.46}$$

where we invoked continuity of F at $\tau = 0$. To calculate E we eliminate $d\tau$ between (104.34) and (104.35) and use the constancy of B to write

$$F\,dF = \tfrac{1}{3}c^2(E - a_R T_2^4)\,d(E - a_R T_2^4) \tag{104.47}$$

whence we have

$$(c/\sqrt{3})(E - a_R T_2^4) = F = F_0 e^{-\sqrt{3}\,\tau}. \tag{104.48}$$

Next we note that (104.38) and (104.39) can be combined to yield

$$F = -\dot{m}R(1 - \eta)(T - T_2)/2\eta_2(1 - \eta - \eta_2). \tag{104.49}$$

But in the downstream flow $\eta \approx \eta_2$, hence (104.49) reduces to

$$F = -\dot{m}R(T - T_2)/\eta_2(3 - \gamma). \tag{104.50}$$

From (104.48) and (104.50) we have

$$T - T_2 = (T_+ - T_2)e^{-\sqrt{3}\,\tau}. \tag{104.51}$$

Furthermore, from (104.40) and (104.50) and the continuity of F at $\tau = 0$ we find

$$T_+ - T_2 = [(3 - \gamma)/(\gamma + 1)]T_-. \tag{104.52}$$

The complete solution implied by (104.41) to (104.52) is sketched in Figure 104.1.
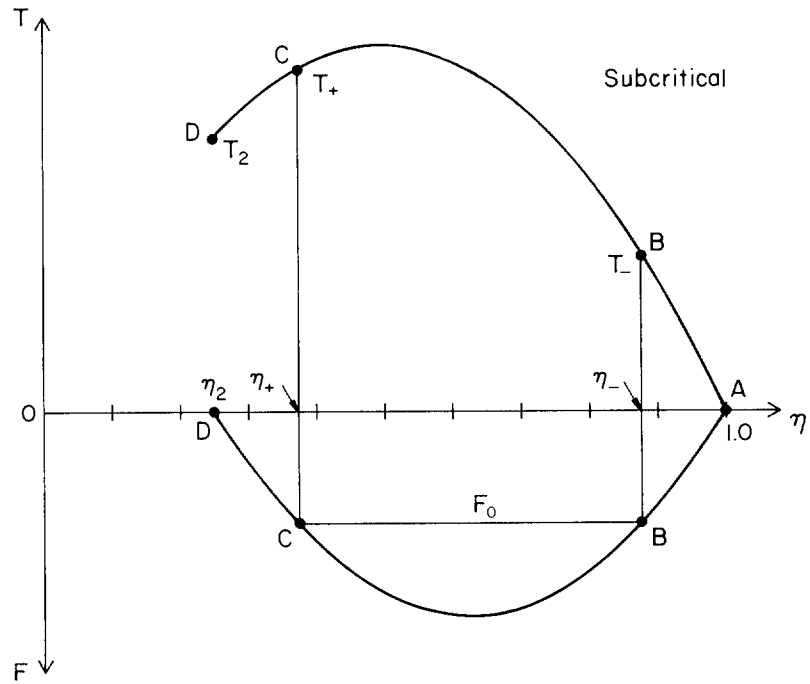
Combining (104.48) with (104.42) at $\tau = 0$ we find

$$E_0 = \tfrac{1}{2}a_R T_2^4 \tag{104.53}$$
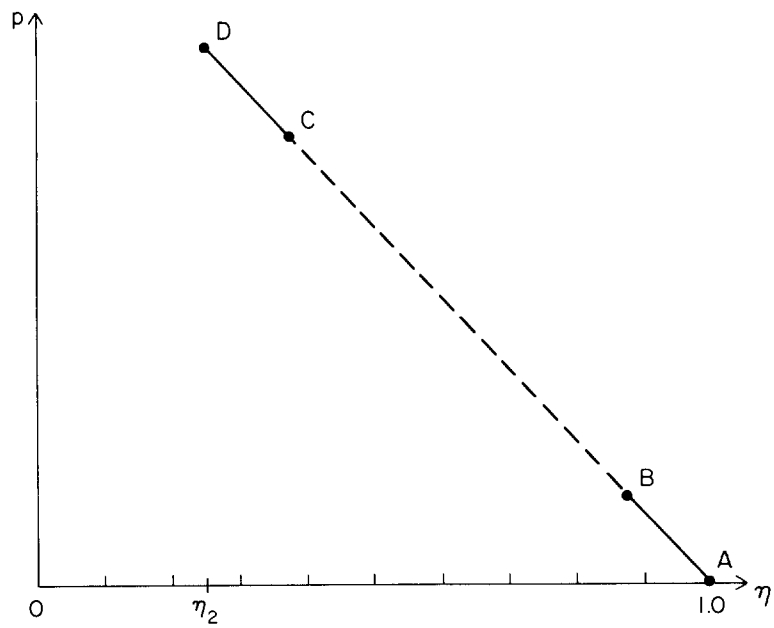
and therefore

$$F_0 = -(2/\sqrt{3})\sigma_R T_2^4. \tag{104.54}$$

T_2 is fixed by the upstream flow speed. Thus evaluating (104.33) at $\eta = \eta_2$ (where $F = 0$) we have

$$\gamma R T_2/(\gamma - 1) = \tfrac{1}{2}u_1^2(1 - \eta_2^2) \tag{104.55}$$

Fig. 104.2 Temperature and radiation flux as a function of volume ratio in a subcritical shock.

Fig. 104.3 Subcritical shock transition in (p, V) diagram.

or

$$T_2 = 2(\gamma - 1)u_1^2/R(\gamma + 1)^2. \tag{104.56}$$

It is instructive to interpret the shock transition in terms of $T(\eta)$, $p(\eta)$, and $F(\eta)$ as given by (104.37) to (104.39) and plotted in Figures 104.2 and 104.3. Starting at point A, at $\eta = 1$, the material evolves continuously to point B, at $\eta = \eta_-$, where F rises to F_0, which is fixed by T_2. For F to be continuous the solution must jump discontinuously to point C, at $\eta = \eta_+$, on the left branch of $T(\eta)$ and $F(\eta)$, such that $F(\eta_+) = F(\eta_-)$. As the maximum of $T(\eta)$, at $\eta = \frac{1}{2}$, lies to the left of the minimum of $F(\eta)$, at $\eta = \frac{5}{8}$, T_+ is substantially larger than T_-; thus the temperature at the front is discontinuous. The material then evolves continuously from η_+ to η_2, and $F \to 0$ while $T \to T_2$. As seen in Figure 104.3, p increases monotonically throughout the entire transition, jumping discontinuously between B and C. Evolution of the solution from C to D along the ascending branch of the $T(\eta)$ curve is possible in the present problem (whereas it was forbidden for the thermally conducting shocks studied in §57) because the radiant energy flux is determined from nonequilibrium diffusion theory, hence F is not constrained to be proportional to (dT/dx) as it is for pure thermal conduction (or equilibrium diffusion).

To make the discussion more quantitative, consider a strong shock in a plasma of completely ionized hydrogen. Then (104.56) becomes

$$T_2 = (3m_H/32k)u_1^2, \tag{104.57}$$

which yields the numerical values listed in Table 104.1. Similarly, using (104.54) in (104.40) we have

$$\dot{m}RT_-/(\gamma - 1) = 2\sigma_R T_2^4/\sqrt{3}, \tag{104.58}$$

or, for ionized hydrogen,

$$T_- = 4\sigma_R T_2^4/3\sqrt{3} \, kn_{p1}u_1 \tag{104.59}$$

Table 104.1. Properties of Strong Shocks in Ionized Hydrogen

u_1 (km s^{-1})	T_-	T_+ (K)	T_2
25.0	3,218	8,711	7,102
26.0	4,235	9,799	7,682
27.0	5,515	11,042	8,284
28.0	7,114	12,466	8,909
29.0	9,095	14,105	9,557
29.5	10,251	15,015	9,889

where n_{p1} is the upstream proton density. Taking $n_{p1} = 10^{17}\,\text{cm}^{-3}$, a reasonable value for the outer envelope of a star, we obtain the results listed in Table 104.1. Finally we obtain T_+ from T_2 and T_- by using (104.52). The numbers in Table 104.1 show the dramatic increase (as u_1^7) of T_- with increasing flow speed.

(c) *Supercritical Shocks*   At some sufficiently large flow speed, u_{crit}, T_- finally equals T_2. We call such shocks *critical shocks* because the structure of the front is quite different in subcritical shocks $(u_1 < u_{\text{crit}})$ and in *supercritical shocks* $(u_1 > u_{\text{crit}})$. We refer to T_- in a critical shock as the *critical temperature*. From Table 104.1 we see that for ionized hydrogen at a density of $10^{17}\,\text{cm}^{-3}$, $u_{\text{crit}} \approx 29.3\,\text{km s}^{-1}$ and $T_{\text{crit}} \approx 9750\,\text{K}$.

According to (104.56) and (104.58), T_- can exceed T_2 when u_1 rises above u_{crit}. This conclusion is erroneous for reasons explained below, and it is important to note that the model developed above becomes invalid before T_- actually reaches T_{crit}. In particular, the analysis assumes that the thermal radiation energy density $a_R T^4$ in the precursor is much smaller than the energy density in the radiation penetrating from the shock. But from (104.53) we see that the two will be equal when

$$T_- = (\tfrac{1}{2})^{1/4} T_2 \approx 0.84 T_2 \qquad (104.60)$$

at which point the model manifestly fails. Thus we cannot trust the model when T_- is above, say, 70 percent of T_{crit}, and it obviously is not able to predict what happens when T_- equals T_{crit}.

A more thorough analysis (Z1), (R1) shows that T_- can never exceed T_2. First, one notes that if $T_- > T_2$, the radiation energy density in the precursor would exceed that in the tail, which would imply $(dE/d\tau) < 0$, hence $F > 0$. But we know from (104.39), which follows directly from the basic conservation laws, that $F \le 0$ everywhere in the flow. Moreover, if T_- were greater than T_2 we would have a closed thermodynamic system in which heat is transferred from low-temperature to high-temperature material, in violation of the second law of thermodynamics. We must therefore conclude that T_- is always $\le T_2$. A rigorous mathematical analysis of the radiation transport equations leads to the same result as these qualitative physical arguments (Z1).

Thus as the mechanical energy of the flow increases above the critical value, the supercritical excess of postshock radiant energy does not force T_- above T_2, but rather drives the radiation precursor more deeply into the upstream flow, producing an extended region with $T \approx T_2$ in front of the shock. The thickness of this zone increases rapidly with increasing T_2.

Viewing the radiant energy transport as a diffusion process we see that in effect a Marshak wave is driven into the preshock material by a radiating "wall" (i.e., the shock) at temperature T_2. In the shock's frame the Marshak wave becomes stationary at the point where material flows into the radiation front at exactly the speed at which the front would otherwise

advance into stationary material. Such an accommodation is always possible because radiation from the "wall" initially moves forward at a significant fraction of the speed of light, but asymptotically a Marshak wave moves forward only as $t^{1/2}$, and thus has a velocity decreasing as $t^{-1/2}$. Radiation at the front of the precursor is out of equilibrium as in a subcritical shock, but rapidly comes into equilibrium as the material temperature approaches T_2.

We can develop an approximate model of the structure of the precursor in a supercritical shock by again using semiquantitative arguments. We divide the precursor into a nonequilibrium zone near the radiation front, followed by an equilibrium zone extending back to the shock. We place the boundary separating these zones at an optical depth $|\tau_c|$ in front of the shock where the thermal radiation energy density equals the actual radiation energy density.

In the nonequilibrium zone we recover (104.40) to (104.43) by the same analysis as before, but with $|\tau|$ replaced by $|\tau - \tau_c|$, and with $F_0 = -(c/\sqrt{3})a_R T_c^4$ in (104.41), $E_0 = a_R T_c^4$ in (104.42), and T_- replaced by T_c in (104.43). Here T_c is the temperature at the boundary between the two zones. We fix T_c by using (104.40) at this boundary, which yields

$$T_c^3 = \tfrac{1}{4}\sqrt{3}\ \dot{m}R/(\gamma - 1)\sigma_R. \tag{104.61}$$

In the equilibrium zone we take $E = a_R T^4$, hence (104.35) becomes

$$F = -\tfrac{16}{3}\sigma_R T^3 (dT/d\tau). \tag{104.62}$$

Combining (104.62) with (104.40) and (104.61) we have

$$T^2\, dT = \tfrac{1}{4}\sqrt{3}\ T_c^3\, d\tau. \tag{104.63}$$

Integrating and demanding continuity at $|\tau| = |\tau_c|$ we obtain

$$\frac{T}{T_c} = \left(\frac{E}{a_R T_c^4}\right)^{1/4} = \frac{\sqrt{3}\,|F|}{4\sigma_R T_c^4} = [1 + (\tfrac{3}{4}\sqrt{3})\,|\tau - \tau_c|]^{1/3}. \tag{104.64}$$

Then using the fact that $T = T_- = T_2$ at $\tau = 0$ we find that τ_c is

$$|\tau_c| = (4/3\sqrt{3})[(T_2/T_c)^3 - 1]. \tag{104.65}$$

From (104.61) and (104.56) one sees that T_2/T_c rises as $u_1^{5/3}$, hence $|\tau_c|$ increases rapidly with increasing shock strength. Because the radiation attenuates exponentially in the nonequilibrium zone, $|\tau_c|$ is essentially the optical thickness of the whole precursor.

Unfortunately, it is not possible to construct a simple, yet realistic, model for the postshock tail in a supercritical shock; nevertheless, a qualitative discussion is worthwhile. From an equilibrium diffusion analysis Prokof'ev (P5) argued that radiative exchange would guarantee continuity of the temperature at the shock front and concluded that a supercritical shock comprises a nonlinear radiation-diffusion front within which is imbedded
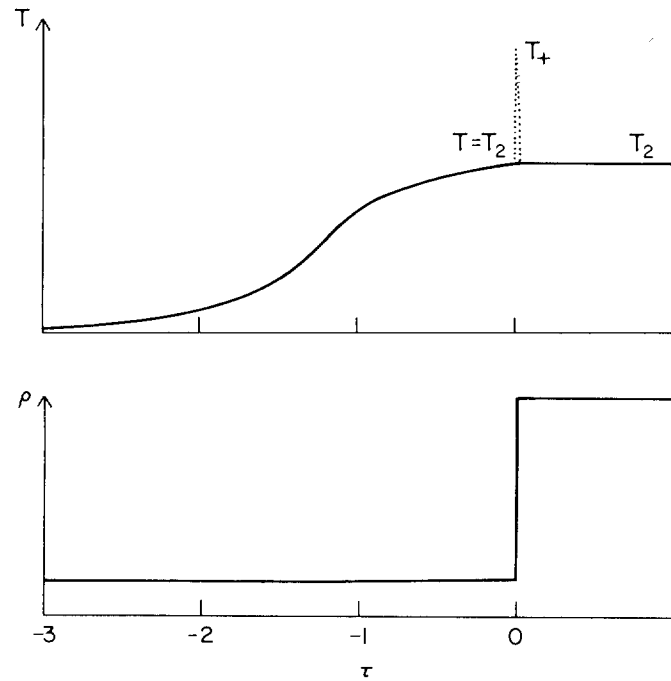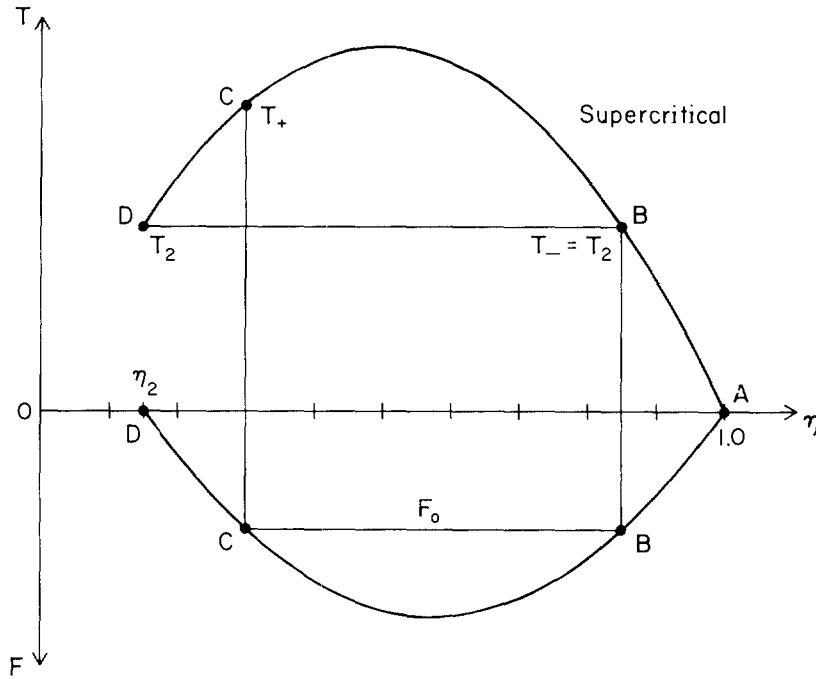
Fig. 104.4 Temperature and density as a function of optical depth in a supercritical shock.

an isothermal shock. At the isothermal shock, the temperature is continuous $(T = T_2)$, but other physical variables jump discontinuously, as sketched in Figure 104.4.

While this picture seems reasonable, it poses a puzzle. We have seen that in subcritical shocks there is a postshock region where T rises to $T_{\_} > T_2$. Moreover, T_+ is a monotone increasing function of T_2. Why should this region suddenly vanish as the shock becomes critical or supercritical? The answer is, it doesn't. Zel'dovich showed (**Z1**) that the temperature distribution in a supercritical shock is *not* continuous. Instead, there is a sharp temperature spike in the downstream flow immediately behind the front (cf. Figure 104.6). As in a subcritical shock, the material in the spike is cooled by radiating into the upstream material. The thickness of the spike turns out to be less than a photon mean free path, and decreases with increasing shock strength; for this reason it is missed by an equilibrium diffusion analysis, which cannot handle properly features on a scale less than λ_p. The spike can be treated correctly only by a detailed transport calculation.

If Prokof'ev's conjecture were true, then in Figure 104.5 the material would evolve continuously from point A to point B, where $T = T_2$, and then jump discontinuously to point D. But, as the curve for $F(\eta)$ shows,

Fig. 104.5 Temperature and radiation flux as a function of volume ratio in a supercritical shock.

the radiation flux would be discontinuous along this path, which is inconsistent with the assumptions underlying the equilibrium diffusion calculation. In reality it is the flux that is continuous (**Z1**). Therefore, in Figure 104.5 the material evolves continuously from A to B, where $F = F_0$, the flux at the front; from (104.64) evaluated at $\tau = 0$ we have

$$F_0 = -(4\sigma_R/\sqrt{3})T_c^3 T_2. \qquad (104.66)$$

The solution then jumps discontinuously, at constant flux, to point C, and finally evolves continuously to point D in a physical distance smaller than a photon mean free path. The temperature jumps discontinuously from T_2 at B to $T_+ > T_2$ at C. We can compute T_+ from (104.38) and (104.39) by demanding that $T_- = T_2$ and $F(\eta_+) = F(\eta_-)$. We find

$$T_+ = (3 - \gamma)T_2. \qquad (104.67)$$

NUMERICAL CALCULATIONS OF RADIATING SHOCK STRUCTURE

The semiquantitative picture of radiating shock structure developed above can be sharpened considerably by recourse to numerical calculation. The classic study was made by Heaslet and Baldwin (**H3**), whose results we summarize here. As before, consider a radiating perfect gas with an

imbedded steady shock and assume that the material is sufficiently opaque that the radiation flux vanishes at upstream and downstream infinity. But we now drop assumptions (1) and (3) of the Zel'dovich–Raizer analysis, and thus allow for the enthalpy and pressure of the upstream material, and use a more accurate solution of the transfer equation.

The equations describing the flow are

$$\rho u = \dot{m}, \tag{104.68a}$$

$$\dot{m}u + p = \dot{m}C_1, \tag{104.68b}$$

and

$$\dot{m}(h + \tfrac{1}{2}u^2) + F = \dot{m}C_2^2 \tag{104.68c}$$

where $\dot{m}$, C_1, and C_2 are constants of integration. F is the radiation flux

$$F(\tau) = 2\sigma_R \left[\int_{-\infty}^{\tau} T^4(\tau') E_2 |\tau' - \tau| \, d\tau' - \int_{\tau}^{\infty} T^4(\tau') E_2 |\tau' - \tau| \, d\tau' \right] \tag{104.69}$$

where

$$\tau(x) \equiv \int_0^x \kappa(x) \, dx. \tag{104.70}$$

As before, we take $\tau = 0$ at the shock, $\tau < 0$ upstream, and $\tau > 0$ downstream; similarly $F < 0$ in the upstream direction.

Nominally (104.69) is a full transport solution for the lab-frame flux, but it omits velocity-dependent terms (cf. §93); similarly terms in E_0 and P_0 have been ignored in (104.68). All of these terms are small unless the temperature in the flow is very high, and can be neglected in the present context. To simplify the analysis, Heaslet and Baldwin use the exponential approximation (V6)

$$E_2(\tau) \approx m e^{-n\tau}, \tag{104.71}$$

with $m = \tfrac{1}{3}n^2$ (which assures recovery of the diffusion limit) and $n = 1.562$.

Introducing a new independent variable $\xi \equiv n\tau$, Heaslet and Baldwin succeeded in reducing (104.68) and (104.69) to a single differential equation:

$$(d^2\theta/d\xi^2) - (\theta - \theta_\infty) = (d\mathcal{F}/d\theta)(d\theta/d\xi), \tag{104.72}$$

where

$$\theta(\xi) \equiv \{[\gamma/(\gamma + 1)] - v(\xi)\}^2 \tag{104.73}$$

with $v(\xi) \equiv u(\xi)/C_1$ and

$$C_1 = u[1 + (1/\gamma M^2)] = \text{constant}, \tag{104.74}$$

and where

$$\mathcal{F}(\theta) \equiv \frac{\mathcal{K}}{4} \left[\frac{\gamma}{(\gamma + 1)^2} + \left(\frac{\gamma - 1}{\gamma + 1} \right) \text{sgn}(\xi) \theta^{1/2} - \theta^4 \right]. \tag{104.75}$$

The solution depends on the two dimensionless parameters

$$\theta_\infty \equiv \tfrac{1}{4}(v_1 - v_2)^2 \qquad (104.76a)$$

and

$$\mathcal{K} \equiv 32m(\gamma - 1)\sigma_R C_1^6/(\gamma + 1)nR^4\rho_1 u_1 \qquad (104.77a)$$

which can be rewritten (**G7**) as

$$\theta_\infty = \tfrac{1}{4}\{[1 + (1/\gamma M_1^2)]^{-1} - [1 + (1/\gamma M_2^2)]^{-1}\}^2 \qquad (104.76b)$$

and

$$\mathcal{K} = \frac{32m\gamma^4}{n(\gamma + 1)}\left(M_1 + \frac{1}{\gamma M_1}\right)^6\left(\frac{\sigma_R T_1^4}{\rho_1 u_1 c_p T_1}\right) = \frac{\mathscr{f}(M_1)}{\mathrm{Bo}}, \qquad (104.77b)$$

where Bo is the Boltzmann number. The parameter θ_∞ is essentially a measure of the shock strength; $\theta_\infty \to 0$ as $M_1 \to 1$, and $\theta_\infty \to (\gamma + 1)^{-2}$ as $M_1 \to \infty$ (approaching 0.141 for $\gamma = \tfrac{5}{3}$ and 0.174 for $\gamma = \tfrac{7}{5}$). The parameter $\mathcal{K}$, being proportional to the inverse of the Boltzmann number, measures the importance of radiation; $\mathcal{K}$ is large when the upstream gas is hot and/or rarefied. $\mathcal{K}$ and θ_∞ are competing parameters because increasing the shock strength tends to steepen the profile, whereas increasing radiation tends to smear it.

Results from a set of computations for a gas with $\gamma = \tfrac{7}{5}$ (diatomic molecules) are shown in Figure 104.6. The computations span the range
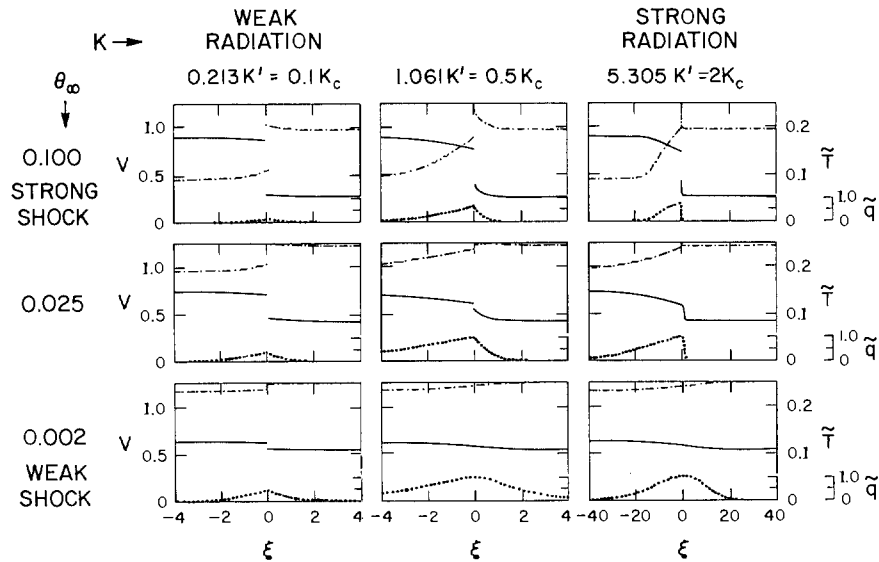
Fig. 104.6 Dimensionless velocity (solid curves), temperature (dash-dot curves), and heat flux (dotted curves) as a function of optical depth in shocks of different strengths and different amounts of radiation. From (**H3**) by permission.

from weak to strong shocks and, at each shock strength, from weak to strong radiation. The plots show the variations of the dimensionless velocity v, temperature

$$\bar{T} \equiv RT/C_1^2 = v - v^2, \tag{104.78}$$

and radiation flux

$$\bar{F} \equiv \frac{(\theta_\infty - \theta)}{\theta_\infty} = \frac{4(v_1 - v)(v - v_2)}{(v_1 - v_2)^2} = \frac{-2(\gamma - 1)}{(\gamma + 1)\theta_\infty \dot{m} C_1^2} F. \tag{104.79}$$

The radiation parameter is stated in units of

$$\mathcal{K}' \equiv 2\sqrt{2}\,(\gamma + 1)^7 \theta_\infty^{1/2}/\gamma^3(\gamma - 1) \tag{104.80}$$

and the "critical" value $\mathcal{K}_c \equiv \frac{3}{2}\sqrt{2}\,\mathcal{K}'$ above which the solution is dispersed by radiation and is therefore continuous unless continuity is precluded by too large a value of θ_∞ (i.e., shock strength).

The bottom row of the figure gives the results for a weak shock $(M_1^2 = 1.20)$. For weak radiation v and $\bar{T}$ are discontinuous, their departures from constancy being antisymmetric about the front, while the radiation flux is symmetric. For moderate and strong radiation the shock is completely dispersed, all variables being continuous; as the radiation parameter $\mathcal{K}$ increases the radiation flux becomes asymmetric, with radiation penetrating deeper into the upstream flow than into the downstream flow.

At intermediate shock strength $(M_1^2 = 2.05)$, shown in the middle row, the shock is discontinuous for both weak and moderate radiation, becoming fully dispersed only at the largest value of $\mathcal{K}$. The asymmetry in the flux becomes very pronounced as the radiation parameter increases. In the strong radiation case there is a small temperature peak a short distance downstream from the front.

The top row shows strong shocks $(M_1^2 = 6.4)$. In the weak radiation case the results differ but little from a classical inviscid strong shock; the radiation flux is symmetric about the front. The moderate radiation case is a good example of a subcritical shock as described by Zel'dovich and Raizer; note that the present, more accurate, calculation shows that the flux distribution is asymmetric about the front. The strong radiation case is a good example of a supercritical shock; for the largest value of $\mathcal{K}$ the upstream material is hot enough that T_- rises to T_2 and a radiation precursor is driven far (i.e., many photon mean free paths) into the upstream material. The flux distribution is strongly asymmetric, and there is a large postshock temperature spike.

Detailed asymptotic analysis of the equations by Heaslet and Baldwin shows that the width of the precursor is proportional to $\mathcal{K}$ while the width of the postshock temperature spike varies as $\mathcal{K}^{-1}$. As remarked by J. H. Clarke (**G7**, p. 281) the latter result can be understood physically by noting that (104.68c) implies an upper bound to the value of $|F|$, namely,

$$-F = \dot{m}(h - h_2 + \tfrac{1}{2}u^2 - \tfrac{1}{2}u_2^2) < \dot{m}(h + \tfrac{1}{2}u^2) \leq m(h_1 + \tfrac{1}{2}u_1^2) \tag{104.81}$$

which can be attained only in the limiting case that the downstream material is absolutely stationary and cold, all of its internal and kinetic energy being converted into radiation flowing upstream. It then follows from (104.69) that if T in the postshock flow is very large, the only way $|F|$ can remain below its upper bound is for the hot region to be *optically thin*, for then $-F \approx \sigma_R T_+^4 \Delta \tau$ where $\Delta \tau \ll 1$ is the optical thickness of the hot region. Thus the postshock temperature overshoot region must collapse to a narrow spike less than one photon mean free path thick. Because T_+ is bounded [cf. (104.67)], the thickness $\Delta \tau$ of the spike does not vanish, but also remains bounded.

Necessary and sufficient conditions for strong shocks to be dispersed by radiative smoothing have been determined by Mitchner and Vinokur (**M12**). They find that in the absence of radiation pressure a sufficient condition for a strong shock in a radiating perfect gas to be discontinuous is that (1) the upstream Mach number exceed the critical value

$$M_1^2 > M_{\text{cr}}^2 \equiv (2\gamma - 1)/\gamma(2 - \gamma), \tag{104.82}$$

or that (2) the upstream gas temperature be sufficiently low. For $\gamma = \frac{5}{3}$, $M_{\text{cr}}^2 = 4.2$, and for $\gamma = \frac{7}{5}$, $M_{\text{cr}}^2 = 2.14$. The intermediate-strength shocks in Figure 104.6 are just below this critical strength, and can be continuous if $\mathcal{H}$ is large, but become discontinuous when $\mathcal{H}$ is small (i.e., the upstream material is cold). Similarly, the strong shocks in that figure are all above the critical strength, hence all are discontinuous.

Mitchner and Vinokur show that the necessary and sufficient conditions for discontinuous shocks can be stated in terms of the upstream Mach number and a dimensionless parameter ψ measuring the influence of radiation. One can show that their $\psi = n\mathcal{H}/4\sqrt{3}\, m$ where $\mathcal{H}$ is defined by (104.77); thus ψ, like $\mathcal{H}$, is proportional to the inverse Boltzmann number. Numerically

$$\psi = 3.39 \times 10^{-12}[(\gamma - 1)/(\gamma + 1)][1 + (\gamma M_1^2)^{-1}]^6 (A^3 u_1^5/n_1) \tag{104.83}$$

where A is the mean molecular weight of the gas in atomic mass units, and n_1 is the upstream particle density.

From numerical integrations Mitchner and Vinokur determine the values $\psi_c(M_1)$ necessary for a continuous shock profile, as shown in Figure 104.7 for various values of γ. For the solution to be continuous ψ must equal or exceed the value implied by the curves. The curve marked "x" indicates the limiting Mach number below which thermal conduction alone can smooth the shock; the curve marked "y" indicates the limiting Mach number given by (104.82), above which all shocks are discontinuous. Necessary *and* sufficient conditions are shown in Figure 104.8; we see that below the critical Mach number M_{cr} continuous solutions are possible if $\psi \geq \psi_c^*$, that is, if the upstream Boltzmann number is sufficiently small. Above that Mach number all solutions are discontinuous.

The effects of viscosity on shock structure in thermally conducting,
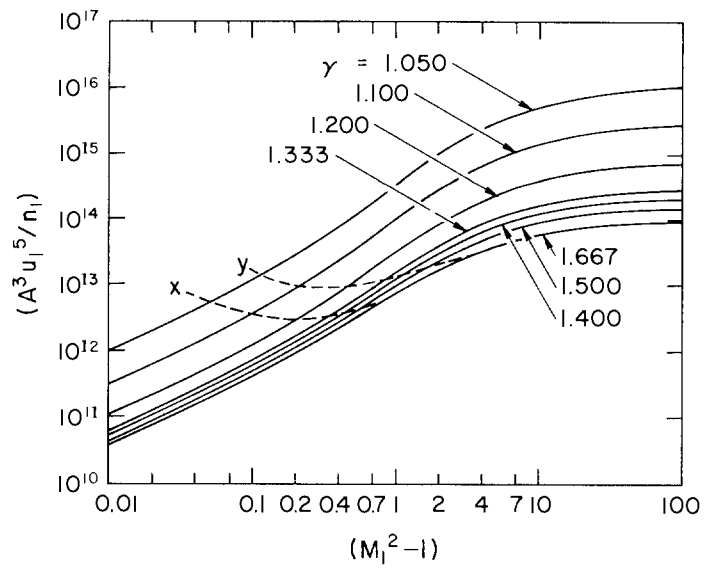
Fig. 104.7 Critical value of radiation parameter necessary for continuous radiating shock transition, as a function of upstream Mach number for various values of γ. From (**M12**), by permission.
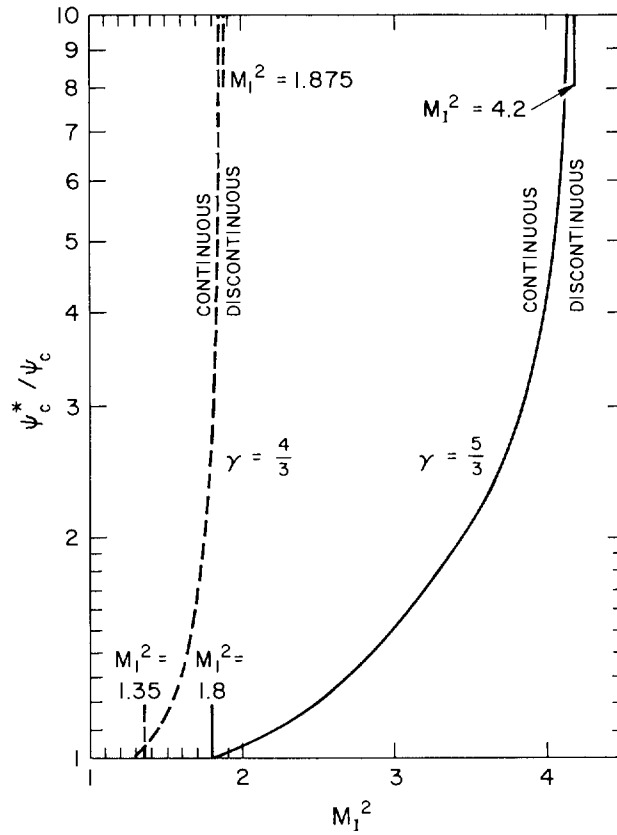
Fig. 104.8 Necessary and sufficient conditions for a continuous radiating shock transition. From (**M12**), by permission.

radiating gases was studied by Traugott. Generally these effects on an isolated shock are small; all the solutions are dispersed by radiation only. The reader can find details in (**T1**).

EFFECTS OF RADIATION PRESSURE AND ENERGY DENSITY ON SHOCK STRUCTURE
The conclusion just stated that shocks above a certain strength are always discontinuous is not strictly correct because we have ignored the pressure and energy density of the radiation. As shown by Belokon (**B3**) and Imshennik (**I1**), (**I2**), when radiation dominates the total fluid pressure and energy density, it is again possible for all variables to remain continuous across the front, even in the absence of viscosity. This remarkable result has direct relevance to astrophysical applications where the upstream material can be both very hot and rarefied, and to very strong shocks that produce enormous postshock temperatures.

To get a physical feeling for the problem, consider an extremely strong shock propagating into cold material. Assume that the radiation and material are in equilibrium so that $E = 3P = a_R T^4$. The shock's structure is described by (104.9) and (104.10), which not only connect initial and final states but also imply that the momentum and energy fluxes are constant throughout the flow. Assume for the moment that $P \gg p$ and $E \gg e$, so that we can neglect p and e. Then (104.9) implies

$$P = \dot{m} u_1 (1 - \eta) \tag{104.84}$$

and (104.10) implies

$$F = \tfrac{1}{2} \dot{m} u_1^2 (1 - \eta^2) - 4 u_1 \eta P = \tfrac{1}{2} \dot{m} u_1^2 (1 - \eta)(1 - 7\eta). \tag{104.85}$$

Equation (104.84) shows that P, hence T, is a monotone increasing function of ρ (hence of x), while (104.85) shows that $F \leq 0$ everywhere in the flow, which is consistent with the monotonic increase of $T(x)$.

From our earlier discussion of subcritical shocks we know that we can always obtain a continuous solution if we can assure that $T(\eta)$ is a monotonic decreasing function of η on the range $\eta_2 \leq \eta \leq 1$ instead of passing through a maximum; hence we infer that shocks with $P \gg p$ and $E \gg e$ will be continuous. But (104.84) is an oversimplification; accounting for gas pressure we have

$$\rho RT + \tfrac{1}{3} a_R T^4 = (\rho_1 RT/\eta) + \tfrac{1}{3} a_R T^4 = \dot{m} u_1 (1 - \eta). \tag{104.86}$$

From (104.86) one sees that $T(\eta = 0) = T(\eta = 1) = 0$, and that $T(\eta)$ actually has a single maximum for some $\eta = \eta_{max}$, $0 \leq \eta_{max} \leq 1$. Nevertheless, if the momentum flux on the right-hand side of (104.86) is sufficiently large, we can assure that $P \gg p$ over nearly the whole range $0 < \eta < 1$. In this event we can force η_{max} to be very small because T^4 grows steadily with $(1 - \eta)$ until η becomes so small that the term $\rho_1 RT/\eta$ finally becomes competitive with $\tfrac{1}{3} a_R T^4$ and thereafter forces T to decrease. In particular we can force η_{max} to be smaller than the smallest physically realizable

value of η (i.e., $\eta_2 = \frac{1}{4}$ when $P \ll p$ and $\eta_2 = \frac{1}{7}$ when $P \gg p$ in a gas with $\gamma = \frac{5}{3}$). T will then be a monotonic decreasing function of η for $\eta \geq \eta_2$, which is the condition needed to obtain a continuous solution.

To determine the shock strength at which the discontinuity first disappears, we force the point $(\eta_{\max}, T_{\max})$ of (104.86) to coincide exactly with (η_2, T_2) at maximum compression. First rewrite (104.86) as

$$\frac{\rho_1 RT}{\eta} + \frac{1}{3}a_R T^4 = \left(\frac{\rho_1 RT_2}{\eta_2} + \frac{1}{3}a_R T_2^4\right)\left(\frac{1-\eta}{1-\eta_2}\right) \qquad (104.87)$$

and adjoin (104.25) rewritten as

$$T_2^3 = (3R\rho_1/a_R)(\eta_2 - \eta_0)/\eta_2\eta_0(1 - 7\eta_2) \qquad (104.88)$$

where $\eta_0 \equiv (\gamma - 1)/(\gamma + 1)$. Differentiating (104.87) with respect to η, setting $(dT/d\eta) = 0$, and demanding that $(\eta_{\max}, T_{\max}) = (\eta_2, T_2) \equiv (\eta_*, T_*)$ we find

$$T_*^3 = (3R\rho_1/a_R)(1 - 2\eta_*)/\eta_*^2. \qquad (104.89)$$

Combining (104.89) with (104.88) we have

$$(14\eta_0 - 1)\eta_*^2 - 8\eta_0\eta_* + \eta_0 = 0, \qquad (104.90)$$

which yields the physically relevant root

$$\eta_* = 1/[4 + (2 + \eta_0^{-1})^{1/2}]. \qquad (104.91)$$

For $\gamma = \frac{5}{3}$, we find $\eta_* = 1/6.45$, close to the limiting value for pure radiation; at this value of η,

$$\alpha_* = (P/p)_* = (a_R/3R\rho_1)\eta_* T_*^3 = 4.45, \qquad (104.92)$$

results obtained by Belokon (**B3**). Shocks sufficiently strong that $\eta_2 \leq \eta_*$ will be continuous.

The analysis above is based on the simplifying assumptions that (1) the gas is a single fluid with all particles in equilibrium at the same temperature, and (2) the upstream material is cold, so that both the radiation and gas pressures are essentially zero. If one relaxes these assumptions one finds (**I1**), (**I2**) that (104.91) yields an upper bound on the compression ratio needed to obtain a continuous solution, and that in fact such solutions can be obtained for a very wide range of upstream flow conditions.

Imshennik considers shocks in a plasma of ions and electrons, with the two species of particles having different temperatures, allowing for radiation pressure and energy density. His results are most conveniently displayed in a plot of the downstream radiation-pressure number $\alpha_2 \equiv (P/p)_2$ as a function of η on a set of Hugoniots corresponding to prechosen values of the upstream radiation-pressure number α_1. In this plot, Figure 104.9, the curve ABC separates continuous and discontinuous solutions. For α_1 less than a certain limiting value $(\alpha_1)_0$, continuous solutions are obtained if the compression ratio r is either less than one critical value or greater than
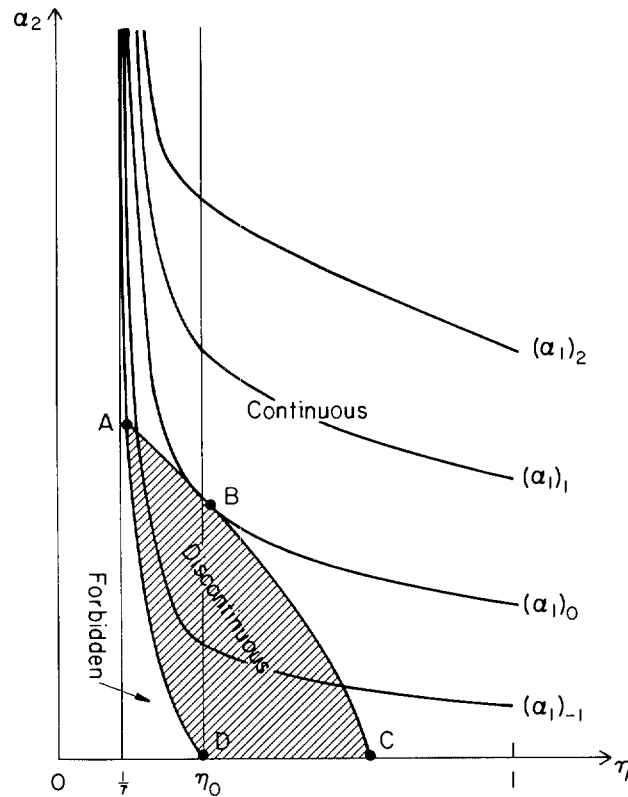
Fig. 104.9 Downstream radiation-pressure number α_2 as a function of volume ratio for radiating shocks with prechosen values of upstream radiation-pressure number α_1. Adapted from **(I1)**.

another critical value, that is, $r \le r_l$ or $r \ge r_u$. As the upstream radiation-pressure number increases, it becomes easier and easier to obtain continuous solutions, that is, r_l increases and r_u decreases. When α_1 just equals the limiting value $(\alpha_1)_0$, $r_l = r_u$, and therefore all shocks with $\alpha_1 \ge (\alpha_1)_0$ are continuous.

Numerical results for r_l and r_u as a function of α_1 in a hydrogen plasma $(Z = 1)$ are given in Table 104.2. One sees that $(\alpha_1)_0 = 2.2774$ and $r_l = r_u = 4.33$ (point B in Figure 104.9); here $\alpha_2 = 3.8249$. When $\alpha_1 = 0$ we find $r_l = 1.1875$ (point C in the figure) corresponding to the critical compression ratio below which shocks are completely dispersed by electron conduction in the absence of radiation (cf. §57), and $r_u = 6.58$ (point A in the figure) corresponding to the limiting shock strength in a cold gas beyond which the shock becomes continuous through the action of radiation pressure alone.

Point A in the limit as $Z \to \infty$ corresponds to the solution found by Belokon. Imshennik obtains $(Z, r_*, \alpha_*) = (1, 6.58, 6.46)$, $(2, 6.56, 5.79)$,

Table 104.2. Critical Compression Ratios for Continuous Radiating Shocks in a Hydrogen Plasma

α_1	r_l	r_u	α_1	r_l	r_u
0.0	1.19	6.58	1.2	2.26	5.97
0.2	1.31	6.47	1.4	2.48	5.83
0.4	1.48	6.39	1.6	2.72	5.67
0.6	1.66	6.30	1.8	3.00	5.47
0.8	1.85	6.20	2.0	3.44	5.22
1.0	2.05	6.09	2.277...	4.33	4.33

$(\infty, 6.45, 4.45)$. As was true for the case of pure electron conduction, the conditions required to guarantee a continuous solution become less stringent with increasing Z (cf. §57).

The curve AD is the Hugoniot for $\alpha_1 = 0$. The region to the left of this curve is "forbidden" because the smallest η to which we can compress a gas with no radiation pressure whatever is $\eta_0 = (\gamma - 1)/(\gamma + 1)$; if we try to go beyond, we generate a nonzero downstream radiation pressure $(\alpha_2 > 0)$ even though $\alpha_1 = 0$ in the upstream flow.

RADIATING SHOCKS IN ISOTHERMAL MATERIAL

Our discussion of radiating shock structure thus far has been predicated on the assumption that the shock is imbedded in an optically thick medium and that all radiation emitted across the front from the hot downstream material is ultimately reabsorbed in the upstream material. The upstream and downstream conditions at large distances from the front are then related by the radiation-modified Rankine–Hugoniot conditions [i.e., (104.8) to (104.10) with $F_{01} = F_{02} = 0$]. But as noted in connection with (104.28) the situation is different if the upstream material is so optically thin that radiation escapes freely to infinity, in which case the temperature jump across the front is smaller, and the density jump is larger, than in an adiabatic shock of the same strength. An extreme case is where the downstream gas radiates away all of the energy of compression across the front and cools back to the original upstream temperature.

In astrophysics the conditions just described actually occur in *gaseous nebulae* where, to a first approximation, the material is essentially in radiative equilibrium in the dilute radiation field of an illuminating star. That is, the temperature of the nebular material is fixed by radiative processes alone, independent of the hydrodynamics, because the radiative heating and cooling rates are orders of magnitude larger than the rate of compressional heating (**O4**, 146), (**S20**, 167). Indeed it is a good approximation to make the idealization that the material remains at *constant temperature* as it passes through the front. More precisely, one is saying that the radiative relaxation zone behind the viscous dissipation zone has a

negligible geometric thickness (i.e., is *unresolvable* telescopically) hence the two zones can be lumped together into a composite front that has the net effect of compressing the gas while leaving its temperature unchanged. Such shocks are usually (but loosely) called "isothermal shocks" in astrophysics; we do not use this terminology because it conflicts with that used in Chapter 5 and in the remainder of this chapter.

We can determine the properties of shocks in isothermal material by formally setting $\gamma = 1$ in (56.40) to (56.43), whence we find

$$T_2/T_1 = 1, \tag{104.93}$$

$$\rho_2/\rho_1 = p_2/p_1 = M_1^2, \tag{104.94}$$

and

$$M_2^2 = 1/M_1^2. \tag{104.95}$$

We see that the density jump across a strong shock in isothermal material can be arbitrarily large rather than approaching a finite upper bound as in an adiabatic shock.

Optically thin shocks are continuously damped by radiative energy loss from the thermodynamically open system, hence the steady-flow model provides only an ephemeral snapshot valid over the time required for an element of material to flow through the shock, be compressed and heated (perhaps ionized), and then radiate and cool (perhaps recombine) downstream. The model provides a caricature of the instantaneous behavior of, say, an isolated pulse in the optically thin layers of a stellar atmosphere. Alternatively it could apply to an optically thin shock continuously driven in a laboratory shock tube.

NONEQUILIBRIUM EFFECTS IN OPTICALLY THIN RADIATING SHOCKS

Skalafuris and Whitney have analyzed the nonequilibrium structure of optically thin radiating shocks in hydrogen (**S12**), (**S13**), (**W6**). [A broader discussion of background physics and approximation schemes can be found in (**C18**).] The shocks are assumed to be steady, and to propagate in an infinite homogeneous medium that is optically thick in the Lyman continuum but optically thin in all subordinate continua. Thus all photons emitted by recombination in the subordinate continua escape to infinity without reabsorption, and the gas temperature downstream returns to the original upstream temperature as described above. Their calculation is more realistic than the picture presented above because it allows for (1) different kinetic temperatures for the various particle species, (2) nonequilibrium ionization and recombination, and (3) radiation transport.

The calculations show that the shock can be divided into four zones: (1) a precursor, which is preheated and partially ionized by radiation from behind the front; (2) an external relaxation zone in which translational equilibrium is established for each particle species; (3) an internal relaxation zone in which ionization equilibrates and the particle temperatures
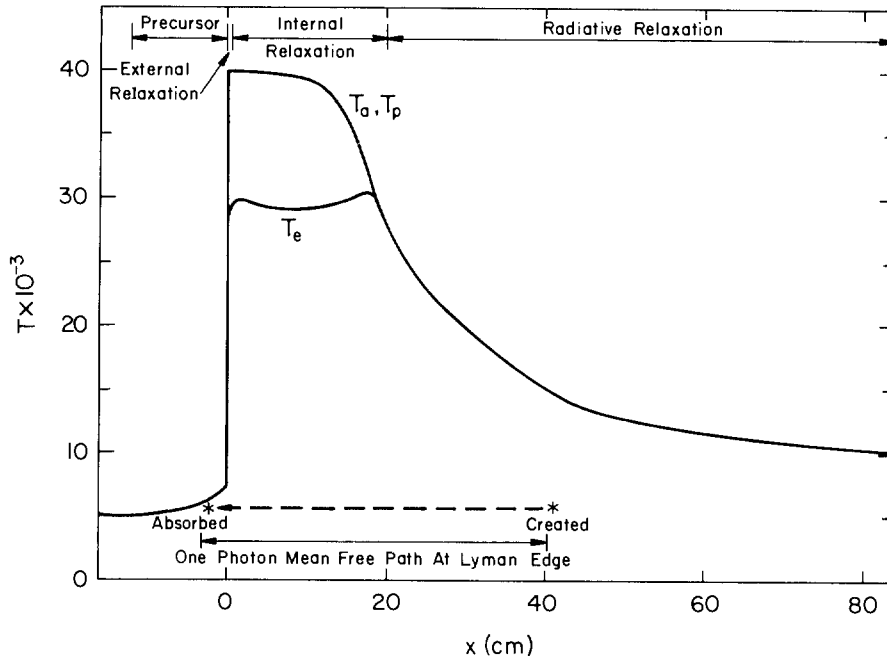
Fig. 104.10 Temperature structure in a nonequilibrium radiating shock. Adapted from (S12), (S13), and (G7).

equalize; and (4) a radiative relaxation zone in which protons and electrons recombine and emit radiation. This structure is sketched in Figure 104.10 for a strong shock propagating at $40\ \mathrm{km\,s^{-1}}$ ($M_1 \approx 5$) into an ambient medium with $T = 5000\ \mathrm{K}$ and $\rho = 2.5 \times 10^{-9}\ \mathrm{g\,cm^{-3}}$ ($n_{\mathrm{H}} \approx 1.5 \times 10^{15}\ \mathrm{cm^{-3}}$).

The cool material in the precursor absorbs Lyman continuum photons, which slightly heats the gas, and the ionization fraction rises from zero to about 0.01 immediately in front of the shock. The external relaxation zone is of essentially zero thickness both geometrically and optically; as discussed in §57 the atoms and ions are strongly heated by viscous dissipation while the electrons are heated by adiabatic compression.

In the internal relaxation region the proton and atom temperatures are locked together by charge-exchange reactions ($\mathrm{H} + \mathrm{H}^+ \rightarrow \mathrm{H}^+ + \mathrm{H}$). The electron gas is cooled by inelastic collisions that ionize atoms (the electrons losing 13.6 eV per ionization from the tail of a Maxwellian distribution with an average energy of only about 2 eV) and are heated by Coulomb collisions with protons. In this region the ionization fraction rises to its equilibrium value (about 0.36) over a distance determined by the collisional ionization rate. The material flows through the entire zone in a time that is short compared to the recombination time, so recombination, leading to photon emission, occurs in a long tail extending far downstream. Indeed, in very strong shocks the postshock plasma is completely ionized

and is too hot to recombine efficiently; it must therefore first cool slowly by free–free emission (bremsstrahlung) before recombination can even begin. As predicted by (104.94), the final compression ratio in these shocks is very large.

It is sobering to note that the calculations by Skalafuris and Whitney show that both the internal relaxation and radiative relaxation zones are at most a few meters thick, which is infinitesimal compared to an atmospheric scale height (10^2 to 10^3 km). It is thus virtually impossible to resolve these features in a general time-dependent flow unless adaptive-mesh techniques are used, because otherwise the zoning required would be prohibitively fine.

105. Propagating Shocks

In §104 we concentrated on how radiation affects the *structure* of steady shocks. We now examine how it affects the *propagation* of shocks via radiative energy exchange (particularly radiative losses) and momentum exchange (i.e., the effects of radiation pressure), and by driving the thermodynamic state of the material away from equilibrium.

WEAK SHOCK THEORY

A complete analytical theory of shock propagation can be constructed for weak shocks (cf. §58). In treating radiative effects, attention has been focused exclusively on radiative energy exchange, and both the effects of radiative forces and the dynamics of the radiation field itself have been ignored. The entropy increase across a weak shock front is given by (56.56), which implies that the heat dissipated by the shock is

$$\Delta q = 2\gamma p_0 m^3 / 3(\gamma + 1)^2 \rho_0, \qquad (105.1)$$

where $m \equiv M_1^2 - 1$. Previously we ignored radiative losses and assumed that Δq went onto raising the temperature of the downstream gas. We now take the opposite extreme view that this energy is all radiated away so that the postshock material ultimately returns to its original temperature.

Different investigators have made differing assumptions about how radiative relaxation behind a weak shock proceeds. For example, in the *Weymann cycle* (**W4**), (**O3**), one assumes that the downstream gas first cools rapidly by radiation at constant density until the specific entropy of the gas returns to its upstream value, and then expands adiabatically back to its original pressure and density. Alternatively, in the *Schatzman cycle* (**S4**) one assumes that the downstream gas first expands adiabatically back to its original upstream pressure (hence to a lower density) and then cools by radiation at constant pressure back to its original density. Both of these cycles are hypothetical and are chosen only because their consequences can be followed analytically; there is no guarantee that either one is an accurate description of reality. For strong shocks, the two cycles convert

different amounts of dissipated heat into radiation [see equations (6.185) and (6.194) in (**B6**)]. However for weak shocks they both give equation (105.1) for Δq.

Using (105.1) for the energy radiated per gram, one can proceed as in §58 to deduce equations governing the propagation of pulses or N waves. Accounting for gradients of temperature, hence sound speed, and of the ratio of specific heats γ, one finds (**U1**) that the variation of the Mach number with height for an N wave is given by

$$\frac{dm}{dz} = -\frac{m}{\Lambda_0} + \frac{1}{2H} - \frac{1}{2}\left(\frac{d\ln\gamma}{dz} + \frac{d\ln a}{dz}\right). \tag{105.2}$$

Allowance for refraction of oblique shocks changes the coefficient of $(d\ln a/dz)$ from $-\frac{1}{2}$ to $-\frac{3}{2}$ (**U1**).

Equation (105.2) can be integrated numerically for a given model atmosphere, and radiative losses as a function of height can then be calculated from (105.1). For example, Ulmschneider (**U1**) has made an extensive set of integrations for representative model solar atmospheres. He attempted to determine the properties of shocks that could be responsible for heating the lower solar chromosphere by comparing computed radiative losses with semiempirical estimates obtained from observation. Setting the shock dissipation rate equal to the observed chromospheric radiative flux, one immediately concludes that within the first 1000 km above the photosphere the radiative losses are easily accounted for by weak shocks ($m \lesssim 0.25$). The required mechanical energy flux, of order $2 \times 10^6 \text{ ergs cm}^{-2} \text{ s}^{-1}$, is only a small fraction of the acoustic flux generated in the subphotospheric convection zone.

The calculations yield an energy dissipation rate that is a sensitive function of the period of the N wave, but that depends only weakly on the input energy flux; hence one can estimate representative wave periods responsible for the heating. Using the best available solar models and estimates of radiative losses one obtains (**U2**) the best fit to the data for periods around 25 to 30 s ($\Lambda \sim 175$ to 200 km). These periods are well below the acoustic-cutoff period in the temperature-minimum region, hence acoustic waves of such periods generated in the convection zone could readily propagate into the chromosphere where they would steepen into sawtooth waves. As remarked in §58, the radiative losses from the waves are severe: over 90 percent of the original wave energy is dissipated at heights below 2000 km.

STRONG LTE SHOCKS

Strong radiating shocks can be studied either with similarity solutions or by direct numerical simulation. We briefly describe here a few representative problems of astrophysical interest.

(*a*) *Similarity Solutions*   Consider first the propagation of a strong, *self-similar radiating shock* moving upward in an exponentially stratified atmosphere (**L6**). Both the high temperatures generated in the accelerating

shock front and the large photon mean free paths (which increase exponentially with height) at high altitudes imply intense, efficient heat transport by radiation, which will tend to obliterate temperature gradients. To obtain an analytically tractable caricature of these radiative effects, one assumes that the postshock material is *isothermal* (in contrast to the case of adiabatic propagation considered in §60). This extremely rough treatment of radiation manifestly cannot be expected to provide a realistic description of radiative effects on a shock.

As in §60, let Z denote the height of the shock, and let $\zeta \equiv z - Z$ be the distance behind the shock, all in units of scale heights. The speed and position of the shock are again given by (60.15b) and (60.17), where t_∞ is given by (60.18). The numerical value of the similarity exponent α will differ from that found in the adiabatic case; it is found to be a function of the shock strength as measured by the volume ratio η_2 across the shock. Jump conditions at the front may be written

$$\rho_2 = \rho_1/\eta_2, \tag{105.3a}$$

$$v_2 = (1 - \eta_2)v_S, \tag{105.3b}$$

and

$$p_2 = (1 - \eta_2)\rho_1 v_S^2. \tag{105.3c}$$

These relations suggest using dimensionless variables $\bar{\rho}$, $\bar{v}$, and $\bar{p}$ defined by

$$\rho(\zeta) = [\rho_1(Z)/\eta_2]\bar{\rho}(\zeta), \tag{105.4a}$$

$$v(\zeta) = [(1 - \eta_2)v_{S0}t_\infty/(t_\infty - t)]\bar{v}(\zeta), \tag{105.4b}$$

and

$$p(\zeta) = [(1 - \eta_2)\rho_1(Z)v_{S0}^2 t_\infty^2/(t_\infty - t)^2]\bar{p}(\zeta). \tag{105.4c}$$

The height variations of these dimensionless variables are found from numerical integration of dimensionless versions of the mass, momentum, and energy conservation equations for isothermal flow, starting from initial conditions $\bar{\rho}(0) = \bar{v}(0) = \bar{p}(0) = 1$. The resulting equations have a singular point; to obtain a unique single-valued solution of the system one must impose a constraint between α and η_2, namely

$$\alpha/(\alpha + 1) = [\eta_2(1 - \eta_2)]^{1/2}. \tag{105.5}$$

The resulting flow-variable distributions for $\gamma = \frac{5}{3}$ are shown in Figure 105.1.

At high altitudes the preshock density is so low that little radiation is absorbed by the upstream gas, which remains cold. The shock therefore approaches its limiting strength, with $\eta_2 = (\gamma - 1)/(\gamma + 1)$; hence

$$1/\alpha \to (\gamma + 1)[2(\gamma - 1)]^{-1/2} - 1, \tag{105.6}$$

from which we find $\alpha = (0.537, 0.885)$ for $\gamma = (\frac{4}{3}, \frac{5}{3})$. The corresponding values for an adiabatic shock are $\alpha = (0.176, 0.204)$. From (60.15b) it then follows that a shock ascends more rapidly in an exponential atmosphere
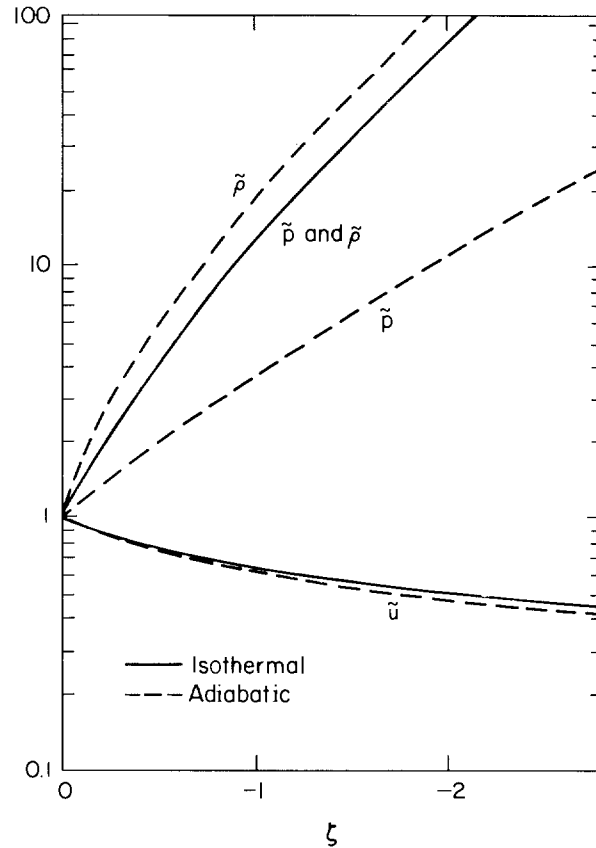
Fig. 105.1 Similarity solutions for radiating shock in an exponential atmosphere. From (**L6**), by permission.

when the downstream gas is isothermal than when it is adiabatic. Higher velocities are reached in the isothermal case because the shock is driven by a larger pressure gradient that develops because the downward flux of radiation from the front raises the temperature, hence pressure, in the dense postshock material, even far from the shock front (**L6**).

Again assuming isothermal downstream material, a similarity solution can also be obtained for power-law density distributions of the form

$$\rho = bx^{\delta}, \tag{105.7}$$

where b and δ are positive constants, and x increases into the medium (**A7**), (**S1**). Equation (105.7) provides a rough caricature of the density distribution in the outer part of a stellar envelope, and thus can be used to study the behavior of a shock emerging from the interior of a star. Taking $t = 0$ to be the instant when the shock arrives at the surface, the shock

position is assumed to be given by

$$X = a(-t)^\alpha. \tag{105.8}$$

Invoking the jump conditions (105.3), one can obtain a solution in similarity form:

$$x = X\xi(\mu), \tag{105.9a}$$

$$v = (1 - \eta_2)\dot{X}\nu(\mu), \tag{105.9b}$$

$$\rho = [\rho_1(X)/\eta_2]g(\mu), \tag{105.9c}$$

and

$$p = (1 - \eta_2)\rho_1(X)\dot{X}^2\pi(\mu), \tag{105.9d}$$

where $\mu = 1$ at the position of the shock, and $\nu(1) = g(1) = \pi(1) = 1$. To obtain a physically meaningful solution through the singular point of the differential equations that determine ξ, ν, g, and π, we must constrain the exponent α. An approximate analytical solution (A7) gives

$$\alpha = \{1 + \delta[\eta_2/(1 - \eta_2)]^{1/2}\}^{-1}. \tag{105.10}$$

The resulting flow-variable distributions for $\gamma = \frac{5}{3}$ are shown in Figure 105.2.
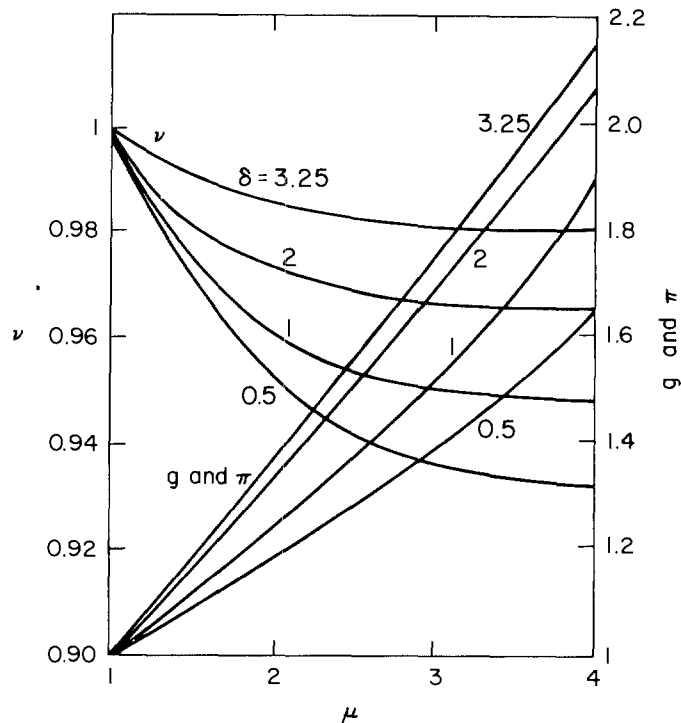
Fig. 105.2 Similarity solutions for radiating shocks in power-law atmospheres. From (S1), by permission.

For a stellar envelope in radiative equilibrium $\delta \approx 3.25$ (**C23**). Using this value of δ and taking the limiting value $\eta_2 = (\gamma - 1)/(\gamma + 1)$ we find $\alpha = 0.348$ for $\gamma = \frac{5}{3}$, which is in good agreement with the more precise value $\alpha = 0.314$ obtained from numerical integration (**S1**). For comparison, the similarity exponent for adiabatic downstream flow (**Z3,** Chap. 12) is $\alpha = 0.590$. From (105.8) one finds that $\dot{X} \propto X^{(1-\alpha)/\alpha}$, hence again the shock velocity is much larger when the downstream material is isothermal than when it is adiabatic.

Similarity solutions for planar radiating shocks driven by a piston are given in (**W1**); these account for radiation diffusion or radiative emission losses in the optically thick and thin limits, respectively. A large number of similarity solutions have been obtained for spherically symmetric radiating blast waves emanating from a point explosion. For example, similarity solutions for very intense explosions in air are given in (**E1**); radiating shocks driven by a piston in planar, cylindrical, and spherical geometry are discussed in (**H4**); a solution for a spherical, radiating, optically thick blast wave in a self-gravitating body such as a star is given in (**O1**); and spherical, radiating shocks in a star with a power-law density distribution are discussed in (**R3**).

While similarity solutions can be used to gain basic insight and to derive scaling rules for the behavior of radiating blast waves, deeper analysis shows that if radiative energy exchange is to be treated at all consistently in either the optically thin or the diffusion limits, then a self-similar solution can be maintained only if the absorption coefficient of the gas varies with a particular power of the temperature and density (**G2**), (**H4**), (**N3**). But the behavior of a material property such as opacity is actually determined by physical laws totally unconnected with the nature of the flow, and usually the requirements for a similarity solution cannot be satisfied. As an example, suppose we assume that the thermal conductivity, Planck mean opacity, and Rosseland mean opacity vary as

$$K = K_0 (T/T_0)^{\beta_C} (\rho/\rho_0)^{\delta_C}, \qquad (105.11a)$$

$$\kappa_P = \kappa_{P0} (T/T_0)^{\beta_P} (\rho/\rho_0)^{\delta_P}, \qquad (105.11b)$$

and

$$\kappa_R = \kappa_{R0} (T/T_0)^{\beta_R} (\rho/\rho_0)^{\delta_R}, \qquad (105.11c)$$

where the subscript zero denotes a convenient reference state. Furthermore, assume that the velocity of the blast wave varies as $\xi^{-\lambda/2}$ where ξ is an appropriate similarity variable; for an adiabatic flow $\lambda = 3$ (cf. §60), and for a momentum-conserving shell $\lambda = 6$. Then, in order to obtain a consistent solution one must demand (**G2**) that the temperature exponents in (105.11) be given by

$$\beta_C = \tfrac{1}{2} - (1/\lambda), \qquad (105.12a)$$

$$\beta_P = (1/\lambda) - \tfrac{5}{2}. \qquad (105.12b)$$

and

$$\beta_R = (1/\lambda) + \tfrac{5}{2}. \tag{105.12c}$$

For an opaque blast wave, the relevant opacity is the Rosseland mean; for a transparent wave it is the Planck mean. Equations (105.12) show that for the values of λ mentioned above β_P must be negative while β_R must be positive. It is extremely unlikely that any real material would have these properties; normally β_P and β_R will have the same sign. Typically β will be positive for a cold gas (e.g., air) that grows more opaque as it becomes excited, dissociates, and ionizes, whereas β will be negative for a hot gas (e.g., in a stellar interior where $\beta_R \approx -3.5$). Thus one can hope to construct a physically consistent solution only for an opaque front in cold material or a transparent front in hot material. An opaque blast in hot material (e.g., a stellar envelope) cannot be treated consistently, for, according to (105.12c), β_R would have the wrong sign.

Thus in many, perhaps most, problems a physically realistic solution will not behave in a self-similar manner. We must therefore turn to numerical modeling; we will discuss a selection of problems of astrophysical interest.

(b) *Shock Heating of the Solar Chromosphere*   Chromospheric shock heating has been studied extensively by Ulmschneider and his co-workers (**U4**), (**K3**), (**U5**), (**U6**), whose results we summarize briefly here. Numerical modeling allows one to remove the limitations of weak shock theory, and to make a detailed calculation of shock heating in realistic atmospheres. The authors just cited solve the Lagrangean equations of continuity and momentum, and a gas energy equation that allows for radiative absorption and emission terms, for vertically propagating acoustic waves (**U5**). The waves are driven into the atmosphere by a periodic piston at the lower boundary. The radiation field is assumed to be quasi-static and all velocity-dependent terms are neglected (**K3**), hence no distinction is made between lab-frame and comoving-frame radiation quantities, and the dynamical behavior of the radiation field is ignored. Similarly, radiation forces are ignored, which is a good approximation in the solar atmosphere. In solving the transfer equation the Eddington approximation (one angle-point quadrature) is made.

The material is assumed to be in LTE, and to be grey with the opacity taken to be the Rosseland mean. The entropy and sound speed are chosen to be the fundamental thermodynamic variables, and the hydrodynamic equations are solved by the method of characteristics with a shock-finding algorithm. As discussed in §59, this method is a bit complicated to implement well; but it has the great advantage that the viscous dissipation zone (which is only a few particle mean free paths thick, hence always optically thin) is represented by a sharp discontinuity of zero optical thickness. In contrast, the standard Lagrangean pseudoviscosity technique smears the shock over several adjacent zones, which may be optically

thick; this method may therefore give a seriously distorted picture of radiative exchange through the shock front. The radiative terms are iterated to consistency with the hydrodynamics at each timestep.

In an initial application of the code, Ulmschneider and Kalkofen (**U4**) studied the propagation and dissipation of short-period waves as perturbations on top of a prescribed (semiempirical) model. This approach does not yield a fully self-consistent final model, but it avoids the necessity of constructing a detailed nongrey, non-LTE, radiative-equilibrium initial model. While the analysis therefore has drawbacks (in particular, it does not handle strong shocks in the fully nonlinear regime quite correctly), it leads to some important conclusions. (1) Heights of shock formation agree with the position of the empirical chromospheric temperature minimum for waves with periods between 25 and 45 s and initial acoustic fluxes between 3×10^7 and 6×10^7 ergs cm^{-2} s^{-1}; both these ranges are in harmony with theoretical predictions of the acoustic spectrum emerging from the convection zone. (2) The mechanical flux in the waves at the height of shock formation agrees well with empirical estimates of chromospheric radiation losses if the waves have periods less than 35 s and initial acoustic fluxes between 2×10^7 and 6×10^7 ergs cm^{-2} s^{-1}. Moreover, such waves explain the observed variation of chromospheric radiation losses with height.

A much more complete ab initio calculation of chromospheric shock heating has been made by Ulmschneider et al. (**U6**). In this analysis the initial model is not fixed as in (**U4**), but is determined from a radiative equilibrium calculation using the hydrodynamic code. The final chromospheric structure is determined from time averages over many wave periods. This procedure has the disadvantage that the initial model represents the solar atmosphere less accurately than the best models that can be produced with a nongrey, multi-angle calculation. However, the disadvantages are outweighed by the fact that we then obtain a self-consistent treatment of the chromosphere's response to shock formation and dissipation. A *differential* comparison of the initial and final models should yield reasonably accurate estimates of the effects of mechanical energy dissipation that are almost independent of the initial model.

The run of physical variables with height is shown in Figure 105.3 for a wave train having a period of 30 s and an initial flux of 5×10^7 ergs cm^{-2} s^{-1}. From Figure 105.3c we see that the average temperature $\bar{T}$ is essentially identical to the radiative equilibrium temperature T_{RE} at heights below about 250 km. Shock dissipation is small at these heights, and in this region of the atmosphere the mean intensity and the temperature merely fluctuate around their radiative equilibrium values. The waves first form shocks at about 590 km, and become fully developed shocks at about 680 km, above which height the atmosphere is strongly heated. At the height of initial shock formation, the waves transport a mechanical flux of 7×10^6 ergs cm^{-2} s^{-1}, having lost much of their original energy by
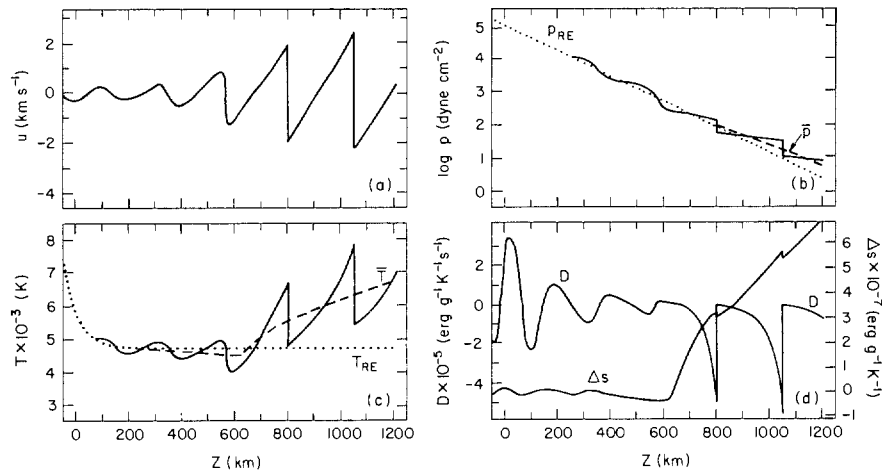
Fig. 105.3 Run of physical variables with height in a model solar atmosphere for a wave train with a period of 30 s. *Dotted curves:* radiative equilibrium temperature and density distributions; *dashed curves:* average temperature and density distributions. From (**U6**), by permission.

radiative damping in the photosphere. The height of full shock development is lower, for a given period, the greater the initial mechanical flux. Hence the larger the input flux, the lower the point of rapid chromospheric temperature rise, and the greater the gas pressure in the chromosphere.

A surprising result of the calculation is that wave dissipation does not invariably heat the atmosphere, but can actually drive the mean temperature *below* its radiative equilibrium value, producing a temperature minimum of about 4370 K at a height of about 640 km. Radiative gains and losses are crucial in this region of the atmosphere, and because both the opacity and the Planck function are strongly nonlinear and the wave-induced temperature fluctuation is large ($\Delta T \sim 500$ K), it turns out that the net rate at which energy is radiated away at a temperature $T_{RE} + \Delta T$ significantly exceeds the net rate at which it is reabsorbed at $T_{RE} - \Delta T$; therefore $\bar{T}$ must fall below T_{RE}. A detailed comparison of the theoretical minimum temperature with empirical models is compromised by the limitations of the calculation (grey material, LTE, monochromatic acoustic waves). Nevertheless, the computations show that the empirical temperature rise in the low chromosphere is easily reproduced for a large range of wave periods and initial mechanical fluxes.

The entropy change Δs of the gas and the net rate of specific entropy generation in the gas by radiation

$$D \equiv (Ds/Dt)_{\text{rad}} = 4\pi\kappa(J - B)/\rho T \qquad (105.13)$$

are shown in Figure 105.3d. The thermodynamic behavior of individual
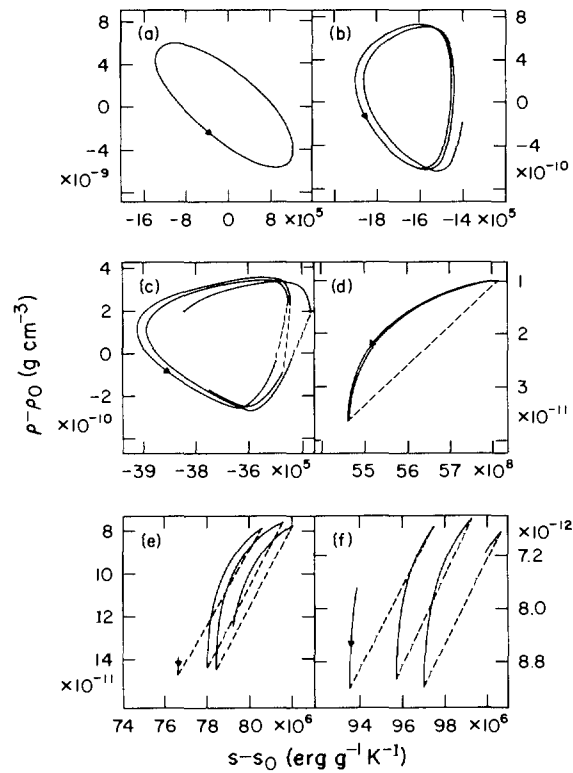
Fig. 105.4 Thermodynamic cycles in (ρ, s) plane. Initial heights: (a) 94 km, (b) 468 km, (c) 624 km, (d) 966 km, (e) 1090 km, (f) 1150 km. From (U6), by permission.

fluid elements can be studied in the (ρ, s) and (p, V) planes as shown in Figures 105.4 and 105.5. The fluid elements displayed there are labeled by their initial heights z_0. Both at great depth where the diffusion approximation is valid and $D \propto (d^2B/dt^2)$, and in the optically thin regime where $D \propto -B$, there is a $180°$ phase shift between D and T, and a $90°$ shift between T and s. The density depends on s and T in such a way as to have a $135°$ phase shift relative to s. Thus low in the atmosphere the thermodynamic path in the (ρ, s) plane is an inclined ellipse, as shown in Figure 105.4a. At greater heights (Figure 105.4b) the shape of the cycle is altered by the nonsinusoidal wave form. Near the temperature minimum (Figure 105.4c) weak shocks develop, which produce a very small entropy change for modest density jumps [cf. (56.56)], hence a nearly vertical jump in the (ρ, s) diagram. As the shock strength increases a larger entropy jump is produced; in Figure 105.4d the material approximately follows the Weymann cycle, with an initial drop in entropy at nearly constant density followed by a nearly adiabatic expansion at constant entropy. At yet
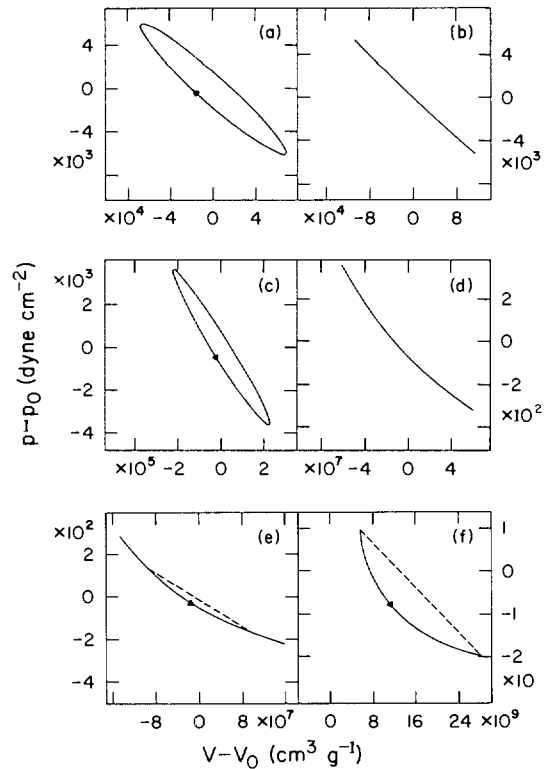
Fig. 105.5 Thermodynamic cycles in (p, V) plane. Initial heights: (a) -44 km, (b) 11 km, (c) 88 km, (d) 550 km, (e) 616 km, (f) 946 km. From (**U6**), by permission.

greater heights (Figures 105.4e and f) a mass element moves continually upward in a mean flow, hence experiences a secular increase in entropy.

From the (p, V) diagrams shown in Figure 105.5 we see that below the photosphere $(\tau > 1)$ the cycles perform positive work (Figure 105.5a) indicating amplification of acoustic waves by the κ mechanism (**C23**, §27.6). At the photosphere, $\tau \approx 1$ (Figure 105.5b) the net work is only marginally positive, and for $\tau < 1$ (Figure 105.5c) the net work is negative, indicating radiative damping. At the temperature minimum, where the net radiative exchange is minimal, the cycle lies nearly along an adiabat (Figure 105.5d). At greater heights (Figures 105.5e and f) the material is heated and compressed by shocks and loses energy by radiation, leading to a negative net work, hence wave damping.

As shown in Figure 105.3a, the velocity amplitude of a shock grows only slowly once it is fully developed, despite the exponential density stratification; the growth is hindered by mechanical energy dissipation coupled to radiative energy losses. The Mach number of the shocks shown in the figure is only 1.5 at a height of 1000 km. As the shocks propagate into the

outer atmosphere they deposit momentum and loft the material; thus the average pressure gradient outward is shallower than in radiative equilibrium (see Figure 105.3b). Mass elements initially below 600 km are not systematically displaced from their original positions. However, after many cycles mass elements initially above 600 km move to average positions some 100 to 150 km higher. Moreover, fluid elements initially above about 1100 km do not arrive at steady average positions, but rise continually, indicating mass loss into a mean outward flow. The existence of a mean flow is consistent with the fact that large-amplitude waves support a net transport of material (**L2**, 252).

Computations of the type just described have also been made for other stars, and appear to explain some of the observed behavior of stellar chromospheres (**U7**), (**S7**), (**S8**), (**S9**). It should be emphasized, however, that solar observations, which reveal strongly enhanced chromospheric emission in magnetically dominated regions (e.g., *plage* and the *chromospheric network*) clearly indicate that the shock-heating theory discussed above provides only a very incomplete description of real chromospheres, adequate at best to explain only the initial temperature rise in the lower chromosphere.

(*c*) *Supernova Explosions*   Type II *supernovae* (**Z4**) are believed to originate when the core of a highly evolved, massive ($\mathcal{M} \geq 5\mathcal{M}_\odot$) star undergoes sudden gravitational collapse and/or a thermonuclear runaway leading to explosive energy release. A total energy of the order of 10^{50} to 10^{51} ergs is released in the star on a time scale short compared to a typical dynamical time scale (e.g., the sound-travel time across the envelope, $\Delta r/a \sim 6$ months), and blows most of the envelope away. A presupernova is expected to have a red supergiant structure comprising (1) a *core* of 1 to $2\mathcal{M}_\odot$ within a radius of 10^7 to 10^8 cm, which collapses to a neutron star or black hole; (2) a *mantle* interior to the helium-burning shell, containing one to several solar masses composed of C, O, Ne, etc. and extending out to 10^{11} cm; and (3) an outer *envelope* composed of He and possibly H (perhaps including an H-burning shell), extending out to 10^{13} to 10^{14} cm. Because supergiants usually show noncatastrophic mass loss in stellar winds, there may also be a circumstellar *shell* containing perhaps $0.01\mathcal{M}_\odot$ and extending out to 10^{15} cm.

As a result of the explosive energy release, and/or because the envelope falls onto the collapsed core and bounces, a very strong shock is driven into the overlying material. The shock is markedly supercritical, hence it drives a radiation front into the upstream gas as discussed in §104. This radiation precursor not only deposits energy and heats the preshock material, but also deposits enough momentum to accelerate the electrons (which then drag along the ions by Coulomb friction) in the upstream gas to high velocities; typically the radiation pressure in the radiative precursor exceeds the gas pressure in the preshock material by one to two orders of

magnitude. Thus the velocity jump across the front is sharply reduced and the shock is strongly radiatively mediated. Indeed the shock is fully dispersed by radiation even in the absence of viscosity, and the radiative diffusive effects are so large that a numerical computation can be carried forward without artificial viscosity for several timesteps without becoming unstable. An exhaustive discussion of radiating shock structure in the diffusion regime for conditions appropriate to supernovae has been given by Weaver (**W2**) for a wide range of shock parameters, and accounting for a large variety of physical phenomena that occur at high energy.

The shock strengthens as it moves outward and runs down the density gradient in the stellar envelope; for a typical velocity of a few thousand $km \, s^{-1}$ it will traverse the envelope in a few hours. An external observer will be unaware that an explosion has occurred until the shock is near optical depth unity at some wavelength; this condition first occurs at high frequencies where the material is more transparent, and the first electromagnetic signal to emerge from the star is a burst of soft X rays lasting about $10^3 \, s$. The luminosity maximum in the visible part of the spectrum does not occur until 4 to 20 days later, depending on whether or not the presupernova is surrounded by a circumstellar shell, when the radiant energy released in the initial event finally escapes by diffusion. As the shock penetrates into optically thin layers the radiation emerging from the front no longer couples efficiently into the upstream material and ceases to accelerate it; the front then steepens into a pure viscous shock that strongly heats the material and drives a hard X-ray burst. Indeed, early calculations (**C19**) assuming compact presupernova envelopes predicted a γ-ray burst and nuclear spallation reactions as the shock unloads in the outer layers. These models did not radiate enough visible luminosity because the material in the blowoff expanded adiabatically and cooled very rapidly; present-day calculations using supergiant presupernovae with extended envelopes easily predict the observed visual luminosities.

As the shocked material expands, it becomes more transparent. The radius of the stellar "photosphere" initially increases as material flows outward, but eventually an external observer will begin to see deeper and deeper into the envelope. When the whole envelope has expanded greatly and becomes transparent the mantle becomes visible; material that has undergone extensive nucleosynthesis is then revealed. Eventually even the mantle becomes transparent as a result of expansion and the compact core remnant (if any) becomes visible.

The radiation hydrodynamics of supernova explosions has been treated by several authors [see e.g., (**C19**), (**L3**), (**C14**), (**F2**)]. One of the most comprehensive discussions is by Falk and Arnett (**F2**), whose results we summarize briefly here. These authors carry out calculations for a variety of initial models, using a one-dimensional spherically symmetric, Lagrangean radiation-hydrodynamics code. The gas is assumed to be a single fluid in LTE. The numerical momentum equation is differenced explicitly

as in (98.16), with pressures and radii time centered as in (59.64) and (59.87), and the pseudoviscosity computed as discussed in §59. In optically deep zones the temperature is updated using an implicit difference representation of the equilibrium diffusion equation (97.7). Near the surface $(\tau \lesssim 5)$ where radiation transport occurs, the temperature is determined by solving the gas-energy equation (98.20) implicitly with the coupled radiation energy and momentum equations (98.5) and (98.8), which are manipulated into the combined moment equation (98.12) and differenced as in (98.34) to (98.36). Thus both the dynamics of the radiation field itself and its dynamical interaction with matter are taken fully into account. The equilibrium diffusion and radiation transport solutions are joined self-consistently by an iteration procedure. Unfortunately the Eddington approximation is made, which compromises the transport solution in optically thin layers and in the extended shell. The material is assumed to be grey. The overall accuracy of the computation is checked by monitoring the total energy conservation law (98.38).

The results are sensitive to whether or not the presupernova is surrounded by an extended circumstellar shell. Consider first a "compact" model representing a $10\mathcal{M}_\odot$ supergiant with a radius of about 2×10^{14} cm and no circumstellar shell. The light curve is shown in Figure 105.6a; note the very sharp initial pulse at $t = 3.4 \times 10^5$ s, in which the luminosity rises over 8 to 10 orders of magnitude in about a day, followed by a broad plateau. The initial postpeak decline results from adiabatic cooling of the rapidly expanding photospheric layers. The plateau results from a period of diffusive energy release in parallel with expansion, cooling, and recombination of the material. The final turndown occurs when recombination in the envelope is essentially complete and the envelope becomes transparent.

Velocity profiles of the material at various times are shown in Figure 105.6b. The shock is just emerging at $t_6 = 0.341$, and one sees the "crack of the whip" effect of shock unloading that accelerates the outer layers suddenly to very large velocities. Velocities continue to rise nearly homologously as radiation continues to perform work on the material for the next few days.

Material temperatures are shown in Figure 105.6c. One sees the dramatic heating of the outer layers by shock emergence (shock positions are indicated by tick marks on the curves for $0.094 \leq t_6 \leq 0.341$). After peak luminosity at $t_6 = 0.341$ the temperature profile is quite flat and the material is continuously cooled by essentially adiabatic expansion. The density structure of the supernova on a mass scale and a radius scale is shown in Figures 105.6d and 105.6e, respectively. The propagation of the shock through the star for $t_6 \leq 0.341$ shows clearly in Figure 105.6d; the nearly invariant density profile at subsequent times results from the nearly homologous expansion in the explosion. The rapid spatial spreading of the ejected material is shown in Figure 105.6e.

Results for an extended model comprising a $5\mathcal{M}_\odot$ supergiant and an
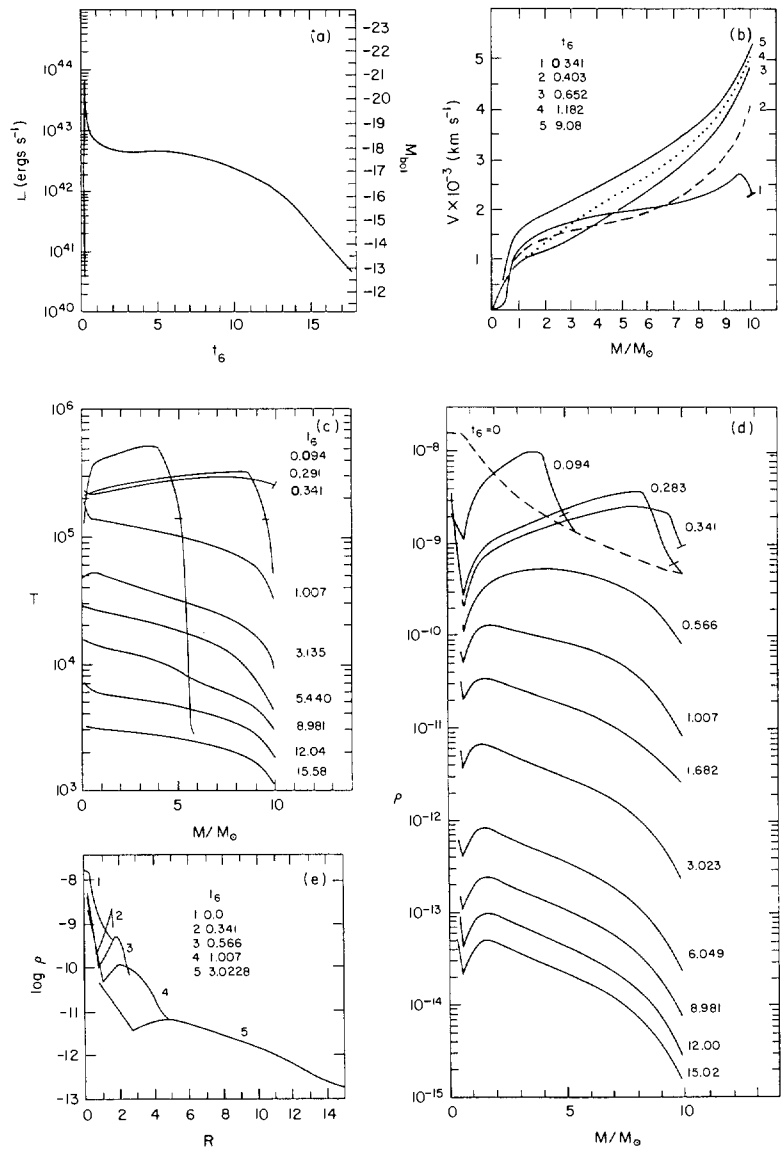
Fig. 105.6 Supernova explosion in a "compact" $10\mathcal{M}_\odot$ supergiant. (a) Light curve. $t_6 = t(\mathrm{s})/10^6$ (b) Velocity as a function of mass. (c) Temperature as a function of mass. (d) Density as a function of mass. (e) Density as a function of radius. From (**F2**), by permission.
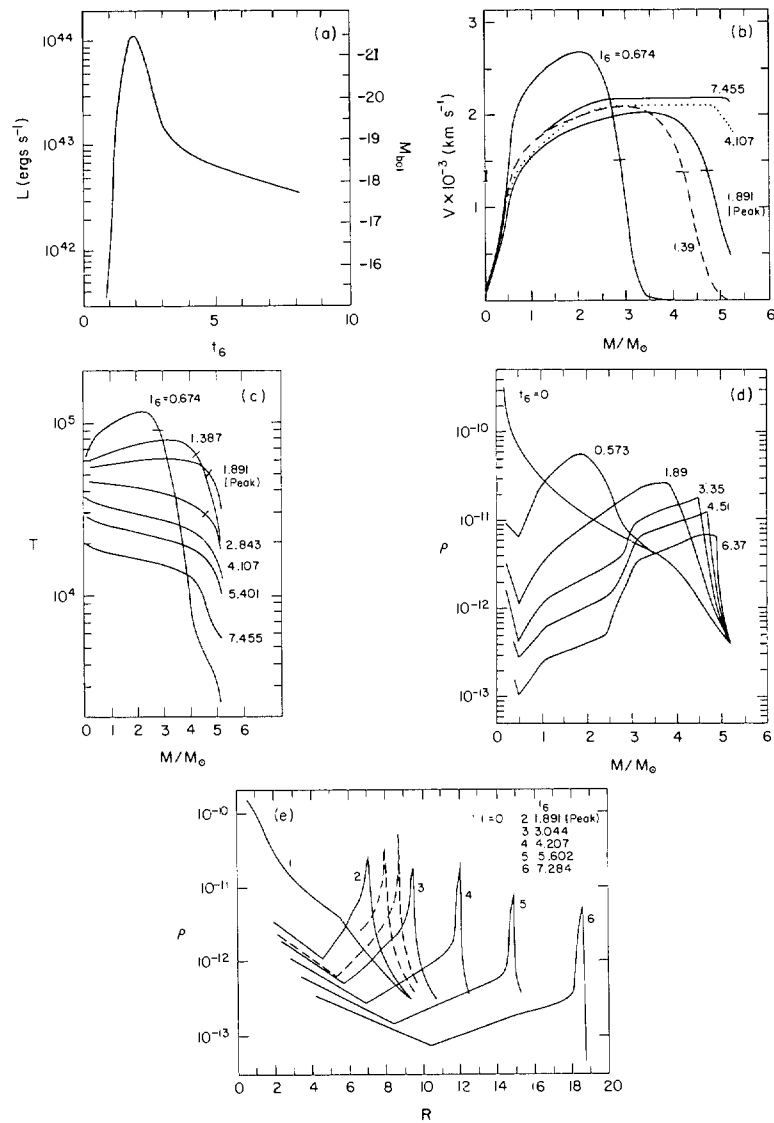
Fig. 105.7 Same as in Fig. 105.6 for extended $5\mathcal{M}_\odot$ model with circumstellar shell. From (**F2**), by permission.

extensive circumstellar shell of radius about 10^{15} cm are shown in Figure 105.7. The light curve, shown in Figure 105.7a, now exhibits a broad peak (width ≈ 20 days), which results when the radiation preceding the shock diffuses through the extended shell. Radiative acceleration and heating of the material is not as efficient as in the compact model, hence the maximum material velocities and peak temperatures are substantially

lower. A striking feature of this model appears in the density profiles shown in Figures 105.7d and 105.7e where we see the formation of a dense, thin shell for $M_r \gtrsim 2.7 \mathcal{M}_\odot$. This shell (qualitatively similar to the structure in a supernova remnant—see below) develops because photons leak efficiently from the low-density outer layers, and therefore the gas pressure does not rise sufficiently to prevent a density inversion (essentially the gas is thermally unstable). The large density inversion is probably Rayleigh–Taylor unstable, hence it may disintegrate into blobs and filaments, mixing several adjacent mass zones and producing large turbulent motions; the development of violent turbulence would bleed energy from the bulk flow. Growth of Rayleigh–Taylor instabilities in the outer layers of supernova ejecta has been explored by Chevalier and Klein **(C15)** using a two-dimensional hydrodynamics code.

Hard X-ray bursts at the time of shock emergence have been predicted by Falk **(F1)** and by Chevalier and Klein **(C16)**, **(K5)** from computations with finely zoned realistic models of the boundary layers. In contrast, Lasher and Chan **(L4)** predict a soft X-ray burst (as do the other authors) but no hard X rays. The essential difference among these calculations is the size of the velocity jump between the emerging shock and the overlying material. In **(F1)**, **(C16)**, and **(K5)** the jump is large and drives a viscous shock that heats the material to order 10^8 K; in **(L4)** the upstream material is radiatively preaccelerated to almost the shock velocity, hence the velocity jump nearly vanishes and the material is never strongly heated. Falk uses the numerical techniques described above **(F2)**, while Chevalier and Klein perform a Lagrangean calculation for a two-fluid (ions and electrons) plasma of ionized hydrogen, treating the radiation dynamics with the nonequilibrium diffusion equation (97.70). A flux limiter (cf. §97) is applied to the flux appearing in the radiative force term in the material momentum equation (96.2), but not to the flux-divergence term in the radiation energy equation (a procedure that is inconsistent). In **(L4)** the radiation is treated by equilibrium diffusion without flux limiting. Chevalier and Klein point out that in optically thin zones the latter approach results in too strong a coupling between the radiation and material, and too large an energy flux, both of which lead to a spuriously large radiative pre-acceleration of the preshock gas.

Epstein **(E3)** has argued that the equilibrium diffusion results are correct and that Chevalier and Klein's calculation is faulty because of their inconsistent use of flux limiting; he suggests that they obtained about the right energy transport, but seriously underestimated the radiative momentum input to, hence acceleration of, the upstream gas. However Chevalier and Klein report **(C16, 603)** that calculations in which the flux limiter was used consistently in both the momentum and radiation energy equations yielded essentially the same results, with only a minor delay in the time of maximum luminosity (which also increased modestly). The controversy can be settled only by a definitive new calculation using the full radiation

energy and momentum equations; but it seems unlikely that equilibrium diffusion with no flux limiting can yield more accurate results than the inherently more complete formulations used in (F1), (F2), (K5), and (C16).

(d) *Supernova Remnants* The evolution of *supernova remnants*, the interstellar material swept up by the blast wave from a supernova, has been analyzed by several authors using similarity solutions (P4), (C21), (C22), and (S20, 200), which do describe many basic features of the flow. Initially the blast wave expands essentially adiabatically, hence its velocity varies as $v_S \propto r^{-3/2}$ [cf. (60.11)]. Eventually the material cools radiatively. A characteristic radiative cooling time is given by the ratio of the material energy density to the rate of radiative energy loss (ignoring reabsorption):

$$t_{rc} \sim \rho c_p T / \sigma_R T^4 \kappa_P, \tag{105.14}$$

where κ_P is the Planck mean opacity. For $t \gtrsim t_{rc}$ a radiative cooling wave penetrates into the material behind the shock front and the nature of the flow changes markedly. In the model of Poveda and Woltjer (P4), it is assumed that the cooling is so efficient that the pressure in the interior of the blast drops essentially to zero; therefore at late times the flow behaves as a momentum-conserving shell that, from simple dimensional arguments, must expand with a front velocity $v_S \sim r^{-3}$. Thus the outer part of the flow collapses into a thin, dense, slowly expanding shell that "snowplows" into the ambient medium, sweeping up a large amount of material.

The treatment of radiative effects in the similarity solutions is highly oversimplified, and a more accurate analysis is needed. Numerical simulations of supernova remnants have been made by Erickson and Olfe (E4) and Chevalier (C13); we discuss briefly some results from the latter calculation, which is based on more realistic physics. The hydrodynamic code solves the momentum equation including gas pressure and magnetic forces. The gas-energy equation includes approximate optically thin radiative gain and loss terms, but no attempt is made to solve realistic radiation energy and momentum equations. The equation of state allows for ionization, and the time variation of the ionization fraction is calculated with a rate equation that allows for photoionization, collisional ionization, and radiative recombination. Magnetic effects prove to be unimportant except in the dense outer shell, which is mostly supported by magnetic pressure. A rezoning scheme eliminates unnecessary inner zones as the calculation progresses, and the accuracy of the calculation is monitored with a total energy check.

The calculation is started by depositing 3×10^{50} ergs as heat in a small region of a uniform medium having a particle density of 1 cm^{-3}; results are displayed in Figure 105.8. The solution quickly relaxes to an adiabatic Sedov blast wave. As the remnant expands, radiative cooling produces a temperature dip behind the shock front by 4×10^4 years; the postshock pressure likewise drops and a density spike emerges. A dense neutral shell
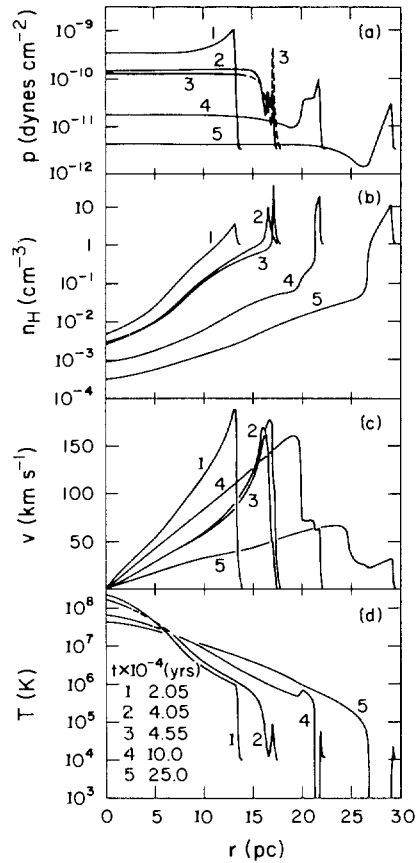
Fig. 105.8 Expansion of a supernova remnant into the interstellar medium. (a) Pressure, (b) hydrogen density, (c) velocity, (d) temperature, all as a function of radius. From (**C13**), by permission.

becomes completely formed by 4.5×10^4 years. Hot, high-pressure inner material accelerates into the pressure low behind the shell, and in fact overtakes the shell and rams into it; shocks then exist on both sides of the shell. The gas is quite cool near the pressure minimum where radiative losses are large, but is reheated to about 10^4 to 10^5 K when it shocks behind the shell. The region where pressure decreases with increasing radius while the density increases is likely to be Rayleigh–Taylor unstable.

The pressure low behind the shell propagates an expansion wave towards the center, which bounces at $t \approx 10^5$ years. Similar, but more extreme, dynamical phenomena are shown in (**E4**).

(*e*) *Accretion Flows* Interesting and complex radiation-hydrodynamic phenomena accompany the *accretion flows* that occur in the gravitational

collapse of a Jeans-unstable protostellar cloud. The basic scenario is that a hydrogen–helium cloud undergoes an initial rapid *collapse phase* (in about one free-fall time) and forms a quasi-hydrostatic core surrounded by a strong radiating shock where the freely falling envelope slams into the core highly supersonically. The cloud rapidly becomes optically thick, hence radiation is trapped, and temperatures quickly rise in the compressed gas. At about 2000 K the hydrogen molecules in the gas begin to dissociate. This process acts as a sink of thermal energy and triggers a second collapse phase because compression of the gas does not produce a rise in temperature, and a corresponding rise in pressure, because the energy is consumed in further dissociation of the gas. Once all the molecules are destroyed, a second low-mass core forms, and a long *accretion phase* ensues in which all matter in the freely falling envelope is accreted by the core.

The problem is extremely challenging because of the immense range of variation of physical quantities that must be followed and because of the presence of extremely strong radiating shocks. For example, as a result of the collapse the central density of the core rises by 20 orders of magnitude, and pressure jumps of a factor of 10^3 across the accretion shock surrounding the core are typical.

An excellent summary and critique of the literature on the formation of a $1\mathcal{M}_\odot$ star is given in (**W7**). The best available calculation is that by Winkler and Newman (**W8**) who use an accurate equation of state, fairly realistic opacities, and a refined version of the advanced numerical techniques of Tscharnuter and Winkler (**T2**). They solve the equations of radiation hydrodynamics implicitly on an adaptive mesh that automatically resolves all important features in the flow. A tensor artificial viscosity [cf. (59.91) to (59.104)] is used to handle shocks. The adaptive mesh is essential to the success of the calculation because individual fluid elements are first stretched by a factor of about 10^5 and then compressed by a similar factor; neither an Eulerian nor a Lagrangean grid would work well under such circumstances. Furthermore the adaptive mesh allows shock fronts to be resolved in optical depth.

The material is assumed to be a grey gas (single fluid) in LTE. Opacities of the gas and of ice-coated "dust" grains are accounted for. The full Lagrangean radiation energy and momentum equations including *all* velocity-dependent terms (cf. §95) are solved using self-consistent variable Eddington factors determined from a full transport computation. The calculations described in (**T2**), (**W7**), and (**W8**) are thus the most complete and consistent treatment of radiation dynamics available in the literature.

The initial model is a cloud of $1\mathcal{M}_\odot$, contained in a radius of 1.5×10^{17} cm with a constant density of 1.4×10^{-19} g cm^{-3}, in thermal equilibrium at 10 K with the ambient interstellar medium. A 10 K thermal radiation field is imposed at the outer boundary. The overall temperature and density structure of the protostar is shown in Figure 105.9 at various stages of the main accretion phase. The tenuous envelope, which contains
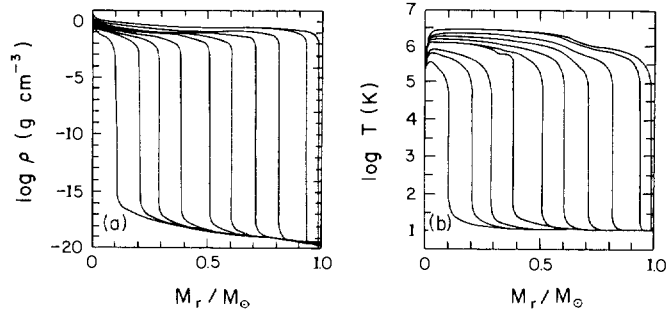
Fig. 105.9 Temperature and density structure in a $1\mathcal{M}$ protostar. Youngest models lie to left, oldest to right. From (**W8**), by permission.

little mass, but runs over several decades in radius, occupies a narrow region in these plots.

Details of the structure near the end of the main accretion phase are shown in Figure 105.10. In the plot of density, Figure 105.10a, four different structural components can be recognized: (1) a centrally con-densed hydrostatic core, (2) an exponential stellar atmosphere between
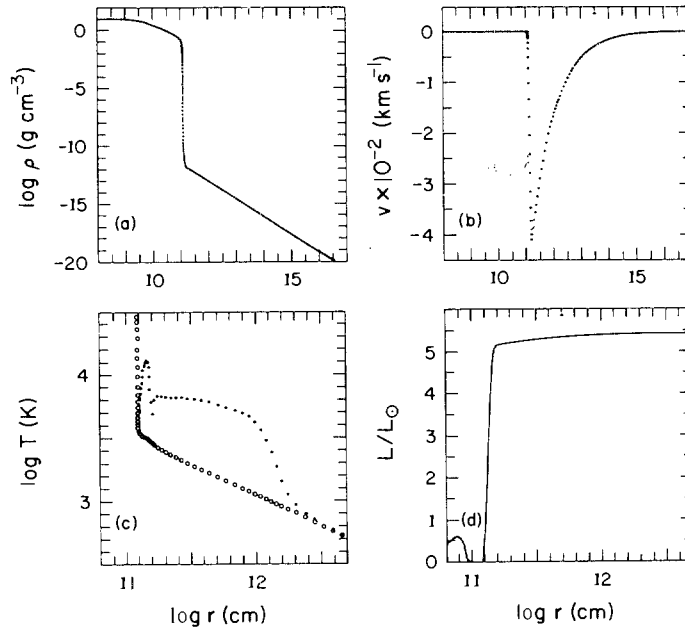

Fig. 105.10 Structure of shock front near end of main accretion phase in a $1\mathcal{M}_\odot$ protostar. (a) Density; (b) velocity; (c) radiation temperature (open circles) and gas temperature (dots); (d) luminosity. From (**W7**) by permission.

$10^{-10} \lesssim \rho \lesssim 10^{-1}$, (3) the accretion shock between $10^{-12} \lesssim \rho \lesssim 10^{-10}$, and (4) the freely falling envelope for $\rho \lesssim 10^{-12}$, in which the density decreases as $r^{-3/2}$. Note that the ten-orders-of-magnitude density drop in the atmosphere is nicely resolved by the adaptive mesh. The position of the shock is identified by the region of maximum pseudoviscous dissipation, and the edge of the core is identified by a sharp maximum in the density gradient $|d \ln \rho / d \ln r|$. The run of velocity with radius is shown in Figure 105.10b. Here we see the free-falling envelope, in which $v \propto r^{-1/2}$, and the sharp velocity discontinuity at the shock near 1.5×10^{11} cm. Again, the velocity jump at the shock front is well resolved by the adaptive mesh.

The radiation temperature, as defined in (97.73), and the material temperature are shown in Figure 105.10c. The gas and radiation are in equilibrium in the core, atmosphere, and outer envelope, but are strongly out of equilibrium in the vicinity of the (smeared-out) accretion shock ($\log r \approx 11.2$) and in the optically thin preshock adiabatic compression zone ($11.3 \lesssim \log r \lesssim 12.3$). As shown in Figure 105.10d, essentially all the kinetic energy of the infalling material is transformed into radiation.

Radiation quantities at various stages in the main accretion phase are shown in Figure 105.11. The run of opacity near the middle of the
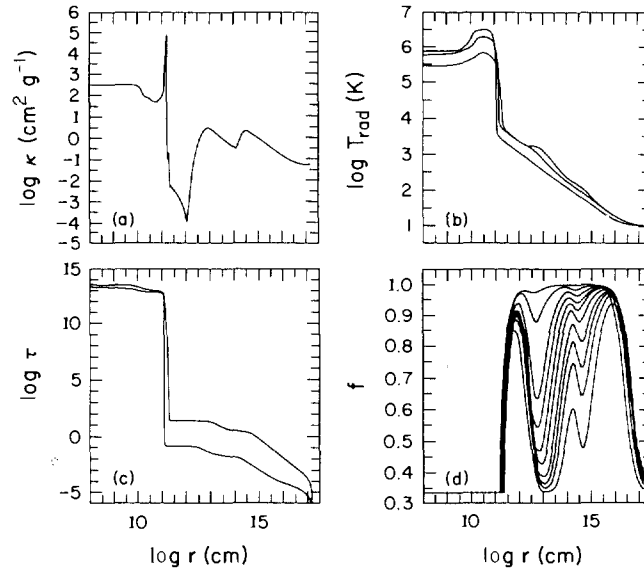
Fig. 105.11 Radiation variables in a $1\mathcal{M}_\odot$ at various stages of main accretion phase. (a) Opacity. (b) Radiation temperature at beginning, middle, and end of accretion phase (bottom to top). (c) Optical depth at beginning and end of accretion phase. Tenuous envelope is optically thick initially and becomes optically thin as it is depleted of material. (d) Eddington factor at various stages of accretion (early at bottom, late at top). From (**W8**), by permission.

accretion phase is shown in Figure 105.11a. Proceeding inward, the opacity first rises to about $1 \, \mathrm{cm^2 \, g^{-1}}$ as the ice mantles on the dust grains absorb, then it drops as these mantles are destroyed at 150 K, rises again as the dust grains themselves absorb, drops again as the dust grains melt at 1600 K, then rises to very large values $(10^5 \, \mathrm{cm^2 \, g^{-1}})$ in the hot shock gas, and finally saturates to a large value in the dense core. Molecular opacities, not accounted for fully in the calculation, could be important in the extensive opacity minimum in the range $11 \lesssim \log r \lesssim 13$. Radiation temperatures at the beginning, middle, and end of the main accretion phase are shown in Figure 105.11b. The run of optical depth near the beginning and end of the accretion phase is shown in Figure 105.11c. One sees a very optically thick core surrounded by an envelope that is initially optically thick but becomes optically thin as essentially all the matter falls into the star.

The run of the variable Eddington factor at various times in the main accretion phase is shown in Figure 105.11d. At the beginning of the accretion phase (lower curve), $f = \frac{1}{3}$ in the core, rises sharply to nearly unity in the optically thin zone at $11 \lesssim \log r \lesssim 13$, drops to $\frac{1}{3}$ again in the opaque zone where the dust grains absorb, rises again at the opacity low near $\log r \approx 14$, drops in the opaque zone where the ice mantles absorb, rises to nearly unity again in the transparent outer envelope, and finally is forced back to $\frac{1}{3}$ again as the stellar radiation field comes into equilibrium with the ambient interstellar field. In contrast, at the end of the accretion phase (upper curve) the Eddington factor rises almost monotonically from $\frac{1}{3}$ in the opaque core to unity in the transparent depleted envelope, and is forced to $\frac{1}{3}$ ultimately only by the imposed radiation at the outer boundary. This complex variation illustrates vividly the essential importance of a *transport* evaluation of the variable Eddington factors, and shows that a non-equilibrium diffusion treatment would be virtually worthless, and that use of an ad hoc flux-limiting procedure would, at best, be of questionable value.
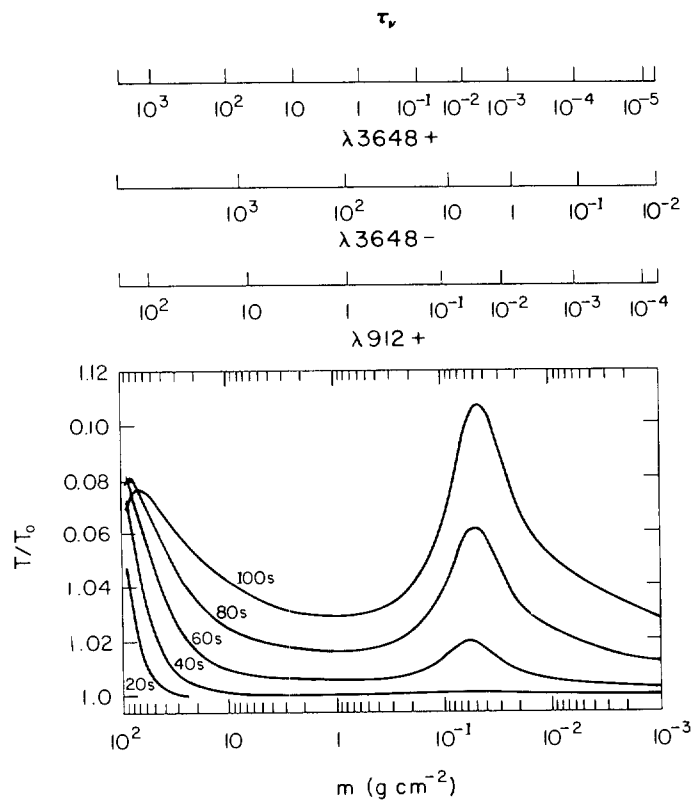
NON-LTE SHOCKS

The solution of the equations of radiation hydrodynamics allowing for departures from LTE for realistic model atoms is quite difficult. One of the most complete efforts of this kind is the work of Klein, Stein, and Kalkofen (**K7**), (**K8**) who consider the propagation of a non-LTE shock driven by a piston that moves with constant velocity into a pure hydrogen atmosphere that is initially in hydrostatic and radiative equilibrium. Here we account for the fact that radiation not only contributes to the energy and momentum balance in the radiating fluid, but also determines the internal excitation and ionization state of the gas.

The computation is performed with a one-dimensional Lagrangean code in planar geometry. The momentum equation is differenced explicitly as in (98.16), (59.64), and (59.87). The energy balance is treated implicitly as in (98.20). In the more refined calculation (**K8**) departures from LTE are

allowed in the first two levels ($n = 1$, $n = 2$), while levels $n = 3$ through $n = 10$ are assumed to be in LTE. Radiative bound–bound transitions are ignored, but all other radiative and collisional processes coupling $n = 1$ and 2 to the continuum and to each other are included. Because the rate equations are very stiff on the relevant dynamical time scales, they are differenced fully implicitly as in (85.40), which follows from (85.39) with $\theta = 1$. The radiation field is assumed to be quasi-static, and the time-independent transfer equation (83.58) is solved implicitly at the advanced time level. Thus the dynamical behavior of the radiation field and the effects of radiative forces are ignored. The frequency dependence of the radiation field is, however, treated (with 15 representative frequencies), and variable Eddington factors are obtained from a full transfer solution; hence the effects of nonlocal radiative energy exchange are handled fairly accurately. This work is probably the best non-LTE shock calculation available in the literature.

The initial model atmosphere has an effective temperature $T_{eff} = 11,500$ K and a gravity $g = 10^4$, appropriate to a late B-type star. A piston is driven into the bottom of the atmosphere (where $\tau_\nu = 200$ at the most transparent wavelength) with a velocity of 4 km s^{-1} ($= a/6$). The piston generates a shock that heats the gas through which it passes and also drives a radiation diffusion wave into the overlying material. The diffusion wave propagates to the surface in about 35 s, which agrees well with the radiative relaxation time of the atmosphere as computed from (100.17) in the optically thick limit. As shown in Figure 105.12, the radiation diffusion wave produces a large temperature rise in a localized region near $\tau_\lambda = 1$ at the head of the Balmer continuum (i.e., at $\lambda 3648^-$ Å). At the adopted effective temperature, the Balmer continuum acts as a net source of heating to the atmospheric material, which maximizes near the characteristic depth $\tau \approx 1$. As the radiation diffusion wave passes that depth, the mean intensity of the radiation field in the Balmer continuum increases significantly, hence the heating rate of the gas is sharply increased. Furthermore, the ambient conditions are such that a rise in temperature happens to increase the opacity in the Balmer continuum, and therefore the rate at which it absorbs energy, leading to a positive feedback effect reminiscent of thermal instability (cf. §100) and the κ-mechanism in pulsating stars (**C23**, §27.6); see also our earlier discussion of Figure 105.5.

The strong localized radiation heat input near $\tau(\lambda 3648^-) = 1$ raises the temperature, hence pressure, of the gas, and drives a compression wave both upward and downward in the atmosphere (Figure 105.13). The downward propagating wave runs into dense stationary material and is quickly damped. The upward-propagating wave accelerates outward and becomes a weak shock, which passes through the uppermost mass zone of the atmosphere at $t = 550$ s; at that point the Mach number in the shock is 1.7 and the density jump is a factor of 2. Although the secondary shock compresses and heats the gas, it is optically thin in the Balmer and higher

τ_ν

$10^3 \quad 10^2 \quad 10 \quad 1 \quad 10^{-1} \, 10^{-2} \, 10^{-3} \quad 10^{-4} \quad 10^{-5}$

$\lambda 3648 +$

$10^3 \quad 10^2 \quad 10 \quad 1 \quad 10^{-1} \quad 10^{-2}$

$\lambda 3648 -$

$10^2 \quad 10 \quad 1 \quad 10^{-1} \quad 10^{-2} \quad 10^{-3} \quad 10^{-4}$

$\lambda 912 +$

$m \ (g \ cm^{-2})$

Fig. 105.12 Thermal precursor wave as function of optical depth at various times after piston is set in motion. From (**K8**), by permission.

$m \ (g \ cm^{-2})$
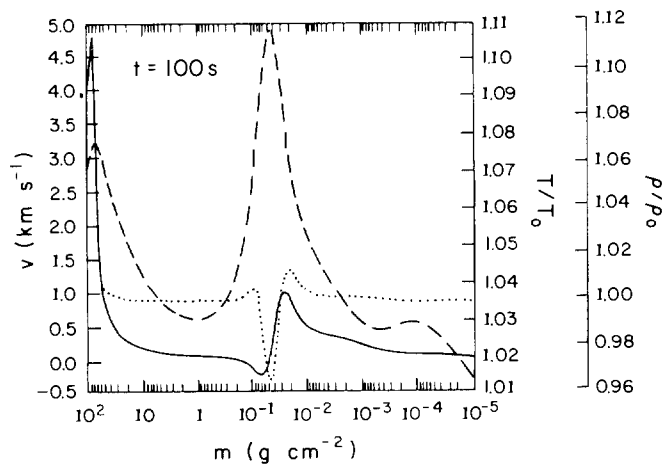
Fig. 105.13 Physical structure of atmosphere at $t = 100$ s. *Solid curve:* velocity; *dashed curve:* temperature; *dotted curve:* density. From (**K8**), by permission.
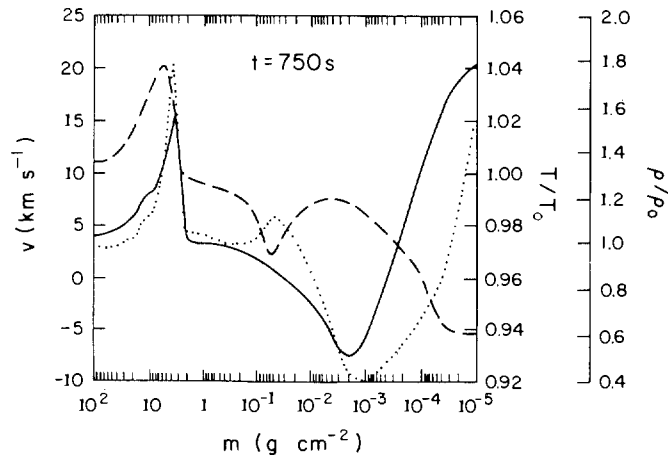
Fig. 105.14   Same as Fig. 105.13 for $t = 750$ s, before accretion shock forms. From (**K8**), by permission.

continua, hence it does not affect the emergent radiation field in visible continua; it would, however, produce detectable effects in the Lyman continuum and in strong spectral lines.

The material that has passed through the radiation-induced compression wave finds itself with insufficient pressure support to maintain it at the height to which it has been carried, hence it free falls back, expanding and cooling quasi-adiabatically (Figure 105.14). The in-falling gas encounters the slowly moving fluid that was not accelerated by the radiation wave and forms an accretion shock at $t = 975$ s (Figure 105.15). This shock produces
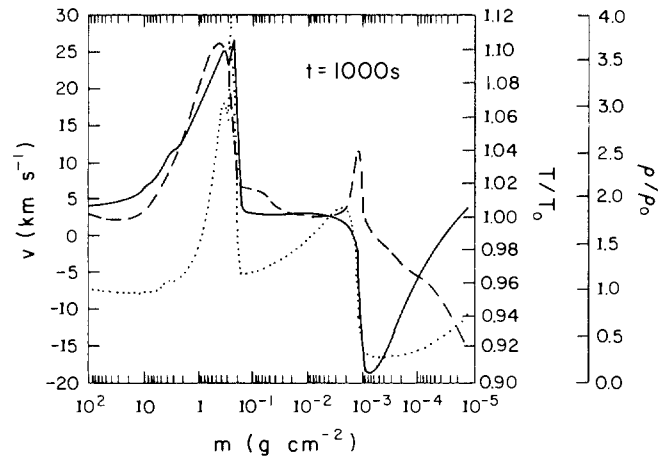
Fig. 105.15   Same as Fig. 105.13 for $t = 1000$ s, after accretion shock forms. From (**K8**), by permission.

a narrow temperature spike that is optically .thin, hence incapable of producing an optical signature except in the Lyman continuum or in strong spectral lines.

The primary piston-driven shock finally emerges at $t \approx 1200$ s. Radiation losses have a profound effect on the propagation of this shock. First, the radiating shock's velocity remains nearly constant, in sharp contrast to an adiabatic shock that accelerates rapidly as it rises. Second, the temperature jump in the radiating shock is quite small, $T_{shock}/T_0 \lesssim 1.2$, in contrast to an adiabatic shock for which $T_{shock}/T_0 \lesssim 2$ to 10. The compression behind the nearly isothermal radiating shock is about a factor of 2 larger than in the adiabatic shock. When the shock finally reaches small optical depth, it cools rapidly. The emergence of the primary shock is essentially invisible in the emitted radiation field. The reason is that shock heating not only raises the source function S_ν locally, but also raises the opacity of the gas, hence shifts the effective radiating surface near $\tau_\nu \approx 1$ [recall the Eddington–Barbier relation (79.17)] outward into cooler gas. The two effects nearly cancel, and an external observer never actually sees the hot shock front until it is already too optically thin to affect the emergent radiation field significantly; precisely the same phenomenon occurs in fireballs from intense explosions, see (R2) and (Z3, 598–626).

A related study has been made by Kneer and Nakagawa (K9) who compute the time development of a nonequilibrium thermal transient in the solar chromosphere. They formulate the problem in terms of implicit Eulerian difference equations, ignoring all velocity-field effects on the radiation field, which is assumed to be quasi-static. They allow departures from LTE in a two-level hydrogen atom including the $Ly\,\alpha$ transition. They also calculate the response of the emergent $Ly\,\alpha$ radiation field to the thermal pulse.

106. Ionization Fronts

In §§104 and 105 we considered flows in which the radiation is essentially driven by the hydrodynamics, as when radiation is created in the high-temperature downstream gas behind a strong shock. In this and the following section we turn to the opposite case where instead the flow (perhaps including shocks) is driven by radiation. Specifically we examine the physics of *ionization fronts* (or *I-fronts*), which occur when intense radiation from a hot source (e.g., an O-star) eats its way into an ambient cold medium (e.g., the interstellar medium). An I-front is an *interface* only a few photon mean free paths thick, across which the material becomes essentially completely ionized while the temperature and pressure jump nearly discontinuously.

An I-front can produce a wide variety of hydrodynamic phenomena. For example, suppose the material is so rarefied and the incident radiation field is so strong that the photon number density is much larger than the particle